iScience

CellPress
OPEN ACCESS

Article

Asymmetric Open-Closed Dimer Mechanism of Polyhydroxyalkanoate Synthase PhaC

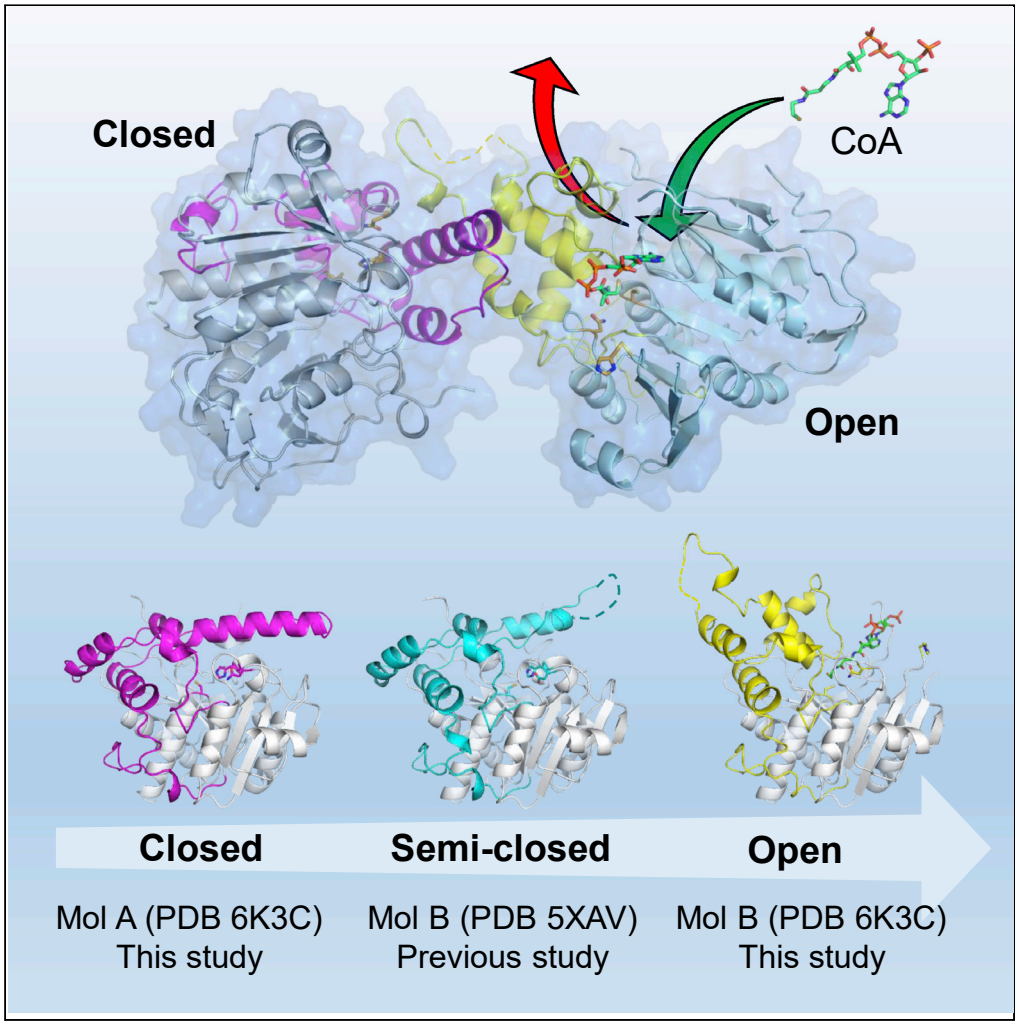

Min Fey Chek, Sun-Yong Kim, Tomoyuki Mori, Hua Tiang Tan, Kumar Sudesh, Toshio Hakoshima

hakosima@bs.naist.jp

HIGHLIGHTS

Crystal structure of PhaC$_{Cs}$-CAT bound to coenzyme A

A unique asymmetric open-closed dimer

Restructuring of the CAP subdomain provides a cleft toward the active site

The cleft enables the substrate entry and the product egress

DATA AND CODE AVAILABILITY

6K3C

Chek et al., iScience *23*, 101084
May 22, 2020
https://doi.org/10.1016/j.isci.2020.101084

iScience

CellPress
OPEN ACCESS

Article

Asymmetric Open-Closed Dimer Mechanism of Polyhydroxyalkanoate Synthase PhaC

Min Fey Chek,[1] Sun-Yong Kim,[1] Tomoyuki Mori,[1] Hua Tiang Tan,[2] Kumar Sudesh,[2] and Toshio Hakoshima[1,3,*]

SUMMARY

Biodegradable polyester polyhydroxyalkanoate (PHA) is a promising bioplastic material for industrial use as a replacement for petroleum-based plastics. PHA synthase PhaC forms an active dimer to polymerize acyl moieties from the substrate acyl-coenzyme A (CoA) into PHA polymers. Here we present the crystal structure of the catalytic domain of PhaC from *Chromobacterium* sp. USM2, bound to CoA. The structure reveals an asymmetric dimer, in which one protomer adopts an open conformation bound to CoA, whereas the other adopts a closed conformation in a CoA-free form. The open conformation is stabilized by the asymmetric dimerization and enables PhaC to accommodate CoA and also to create the product egress path. The bound CoA molecule has its β-mercaptoethanolamine moiety extended into the active site with the terminal SH group close to active center Cys291, enabling formation of the reaction intermediate by acylation of Cys291.

INTRODUCTION

The production of petroleum-based (petrochemical) plastics releases tons of greenhouse gases and leaves undesirable visual footprints in the environment after their disposal such as microplastics in marine environments and the disruption of natural ecosystems (Hopewell et al., 2009; Jambeck et al., 2015; North and Halden, 2013). One promising candidate for replacing petrochemical plastics is polyhydroxyalkanoate (PHA), which possesses comparable properties such as thermal stability and elastomeric properties (Chen and Patel, 2012; Rehm, 2003; Sudesh et al., 2000). There is tremendous interest and research activity from both research community and industry in utilizing PHAs in a variety of areas such as the production of straws, packaging, cosmetics, agriculture, pharmacology, and medicine (Park et al., 2005; Williams and Martin, 2005; Zinn et al., 2001). PHAs are polyesters biosynthesized by various bacteria and halophilic archaea using renewable resources like oils, sugars, plant biomass, and carbon dioxide (Lau et al., 2014; Snell et al., 2015; Stubbe et al., 2005; Wang et al., 2013). PHAs are biodegradable in soils and oceans (Doi et al., 1992; Mergaert et al., 1993). When the environment consists of excess carbon sources with limitations in other nutrients, PHAs are synthesized as water-insoluble granules in cells for storage as carbon reserves, so that when carbon becomes limited in the surrounding environment, these stored granules are degraded by PHA depolymerase (PhaZ) (Anderson and Dawes, 1990; Gao et al., 2001).

To date, 14 PHA biosynthesis pathways have been reported (Meng et al., 2014), and the key enzyme PHA synthase (PhaC) has been identified as being responsible for polymerizing the monomeric hydroxyalkanoate substrates (Peoples and Sinskey, 1989; Rehm, 2003; Schubert et al., 1988). The enzymes have been categorized into four major classes, Classes I–IV, based on their primary sequences, substrate specificity, and subunit composition (Pötter and Steinbüchel, 2005; Rehm, 2003). Class I, III, and IV synthases favor short-chain-length (SCL) monomers comprising C3-C5 carbon-chain lengths as substrates, such as (*R*)-3-hydroxybutyrate (3HB), a typical C4-carbon-chain-length substrate. In all classes, PhaC catalyzes attachment of the acyl moieties of 3-hydroxybutyryl-coenzyme A (3HB-CoA) to the high-molecular-weight PHA product polyhydroxybutyrate, with concomitant release of CoA (Figures 1A and 1B). Class II synthases tend to consume medium-chain-length (MCL) monomers comprising C6–C14 carbon chain lengths, such as the C6 monomer 3-hydroxyhexanoate (3HHx).

PHA comprising mixtures of SCL and MCL monomers possesses better thermal and physical properties than homopolymers. To synthesize PHA with higher MCL content, protein engineering of PhaC has been performed with the hope of broadening its substrate specificity (Chek et al., 2019; Doi et al., 1995;

[1]Structural Biology Laboratory, Nara Institute of Science and Technology, 8916-5 Takayama, Ikoma, Nara 630-0192, Japan

[2]School of Biological Sciences, Universiti Sains Malaysia, 11800 Penang, Malaysia

[3]Lead Contact

*Correspondence: hakosima@bs.naist.jp

https://doi.org/10.1016/j.isci.2020.101084

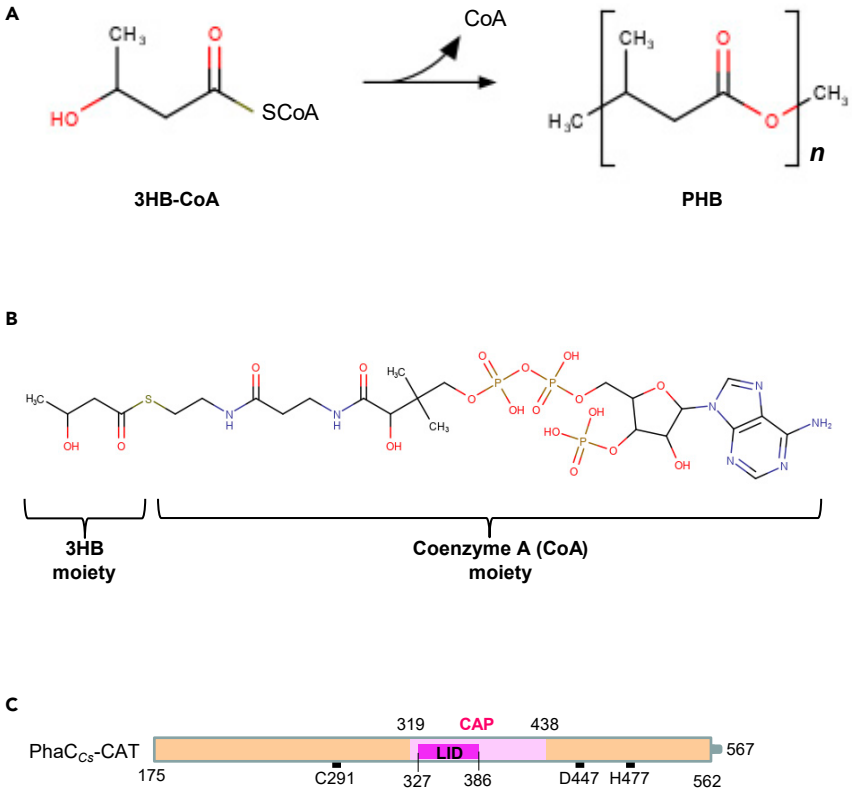

Figure 1. PhaC Catalyzes PHA Biosynthesis

(A) PhaC catalyzes polymerization of 3-hydroxybutyryl coenzyme A (3HB-CoA) into poly 3-hydroxybutyrate (PHB) with concomitant release of CoA.

(B) Chemical structure of 3HB-CoA.

(C) Domain organization of the C-terminal catalytic (CAT) domain of PhaC$_{Cs}$. PhaC$_{Cs}$-CAT (residues 175–567) comprises the α/β core subdomain (residues 175–318, 439–562 in orange) and the α-helical CAP subdomain (residues 319–438 in pink), which contains the LID region (residues 327–386 in magenta). The α/β core subdomain contains the conserved active site including triad residues Cys, His, and Asp.

Taguchi and Doi, 2004). Alternative studies to isolate other naturally evolved synthases with better enzyme performances have been performed and resulted in the isolation of modified PhaC enzymes such as a Class I PHA synthase from *Chromobacterium* sp. USM2 (PhaC$_{Cs}$), which is able to produce poly(3-hydroxybutyrate-*co*-3-hydroxyhexanoate) [P(3HB-*co*-3HHx)] copolymer and poly(3-hydroxybutyrate-*co*-3-hydroxyvalerate-*co*-3-hydroxyhexanoate) [P(3HB-*co*-3HV-*co*-3HHx)] terpolymer (Bhubalan et al., 2010a, 2010b). In addition, PhaC$_{Cs}$ has also demonstrated better enzymatic performance than the typical Class I synthase from *Cupriavidus necator*, PhaC$_{Cn}$ in both *in vitro* and *in vivo* studies (Bhubalan et al., 2011).

Recently, we have determined the crystal structure of the catalytic domain (residues 175–567) of PhaC$_{Cs}$ (PhaC$_{Cs}$-CAT) in a free state at 1.48 Å resolution (Chek et al., 2017) (Figure S1A). The structure showed that the enzyme forms an α/β hydrolase fold comprising α/β core and CAP subdomains with catalytic residues Cys291, Asp447, and His477 at the active site, which is located at the bottom of the cleft of the α/β core subdomain. In the crystal, PhaC$_{Cs}$-CAT forms a symmetrical homodimer and adopts a closed conformation with the active site covered by the LID region (Pro327-Pro386) of the CAP subdomain (residues 319–437) (Figure 1C), so as to block substrate entry. Structures of the catalytic domain from PhaC$_{Cn}$, (PhaC$_{Cn}$-CAT) in the free state were determined by two other groups at 1.80 Å resolution (Kim et al., 2017; Wittenborn et al., 2016) (Figure S1B). The PhaC$_{Cn}$-CAT structure showed another dimeric form with conformational changes in the CAP subdomain, which may be induced by artificial disulfide bond formation in the crystallization as discussed (Chek et al., 2017). The previously reported partial crystal structure, however, disclosed limited information on its catalytic mechanism. Two major models of catalytic mechanisms for PhaC were proposed based on their elongation process in PHA biosynthesis (Hiroe et al., 2019; Sagong

et al., 2018; Stubbe et al., 2005). One required two catalytic Cys residues for elongation of the substrates though the ping-pong mechanism, which is also known as the *non-processive model* (Figure S2A), whereas all three reported crystal structures of PhaC dimers showed that the catalytic Cys residues are located too far apart from each other for the elongation process to happen. Contrastingly, the other proposed mechanism, also known as the *processive model*, required only a single catalytic Cys residue for the elongation of the polymers (Figure S2B). Despite the breakthrough discoveries, the structural information is still limited to decipher the complex mechanism of PhaC as the free form structures representing an inactive status.

In this study, we report on the co-crystal structure of PhaC$_{Cs}$-CAT and CoA at 3.1 Å resolution. The complex structure revealed an asymmetric dimer wherein one protomer adopts a closed conformation whereas the other CoA-bound protomer adopts an open conformation; these interact with each other through their CAP subdomains. Comparison of the closed and open conformations reveals a dynamic conformational change in the CAP subdomain, which facilitates entry and binding of CoA to the active site. The open conformation showed a clear substrate entry pathway and possible binding pockets for acyl moieties of the substrates. Our structure reveals a valuable snapshot of the catalytic activity of PhaC and contributes to an understanding of the mechanism by which dimerization facilitates PhaC polymerase-mediated production of PHA polymers.

RESULTS

Preparation and Structural Determination of PhaC$_{Cs}$-CAT Bound to CoA

CoA has an inhibitory effect on PhaC catalytic activity due to the by-product released from the substrate acyl-CoA (Gerngross and Martin, 1995; Ushimaru et al., 2013). The CoA moiety of acyl-CoA substrates is important for PhaC activity as PhaC$_{Cn}$ could not catalyze substrate analogs that lacked the adenosine 3′,5′-bisphosphate or 3′-phosphate moiety in 3HB-CoA (Gerngross and Martin, 1995; Ushimaru et al., 2013). Another inhibition study using PhaC-PhaE (class III) from *Allochromatium vinosum* (PhaCE$_{Av}$) showed that the CoA moiety is essential for substrate binding (Zhang et al., 2015). These results suggest that the CoA moiety of substrate acyl-CoA participates in interactions with PhaC that forms the PhaC-substrate complex. In our pursuit of an intermediate complex, co-crystallization with CoA using wild-type or various mutated (and subsequently catalytically modified) PhaCs was attempted. We found that PhaC$_{Cs}$-CAT with a mutation of Asp447 to Asn, PhaC$_{Cs}$(D447N)-CAT, is able to form a complex crystal with CoA. The complex structure was solved by molecular replacement using the free form structure of PhaC$_{Cs}$-CAT (Chek et al., 2017) as a search model (Table S1).

The PhaC$_{Cs}$-CAT Heterodimer Formed by the Free and CoA-Bound Forms

The crystal structure of the complex between CoA and PhaC$_{Cs}$(D447N)-CAT was determined at 3.10 Å resolution. Hereafter, PhaC$_{Cs}$(D447N)-CAT is referred to as PhaC$_{Cs}$-CAT for simplicity. We found two crystallographically independent PhaC$_{Cs}$-CAT molecules in the lattice. Both PhaC$_{Cs}$-CAT molecules display the α/β hydrolase fold comprising the α/β core and α-helix-rich CAP subdomains (Figure 2). However, to our surprise, these two molecules exist in distinct forms and adopt different conformations, where one protomer is in a CoA-free form (Mol A) and adopts a closed conformation, in which the CAP subdomain covers the active site, whereas the other protomer is in a CoA-bound form (Mol B) and adopts an open conformation, in which the active site is uncovered by removing the CAP subdomain. The conformation of the CAP subdomain of the CoA-bound form is distinct from that of the CoA-free form (see details below). Intriguingly, the CAP subdomains in different conformations interact with each other to form an asymmetric 1:1 heterodimer comprising the free and CoA-bound forms. Structural comparison of the dimeric arrangement of our heterodimer with reported homodimers in the free forms revealed three different dimeric arrangements (Figures S1A–S1C). The homodimer of PhaC$_{Cs}$-CAT in the free form has a pseudo dyad symmetry, and both protomers display essentially the same closed conformation (Figure S1A) (Chek et al., 2017). Another free form of PhaC$_{Cn}$-CAT forms a symmetrical homodimer with the crystallographic dyad axis (Figure S1B). These two free forms display a rearrangement of dimer interfaces resulting in a swing shift of ~40 Å and a rotation of ~120° as previously analyzed (Chek et al., 2017) (Figure S1D). Compared with these homodimers, our PhaC$_{Cs}$-CAT heterodimer displays a further dynamic shift in dimerization. If the free form (Mol A) of the PhaC$_{Cs}$-CAT heterodimer is superimposed on Mol A of the PhaC$_{Cs}$-CAT homodimer, the CoA-bound form (Mol B) is swung by ~40 Å with a rotation of ~90° (Figures S1C and S1D). This swing shift is in the opposite direction from that of the PhaC$_{Cn}$-CAT homodimer. The rearrangement of dimer association is induced by conformational changes in the CAP subdomains, as previously discussed (Chek et al., 2017).

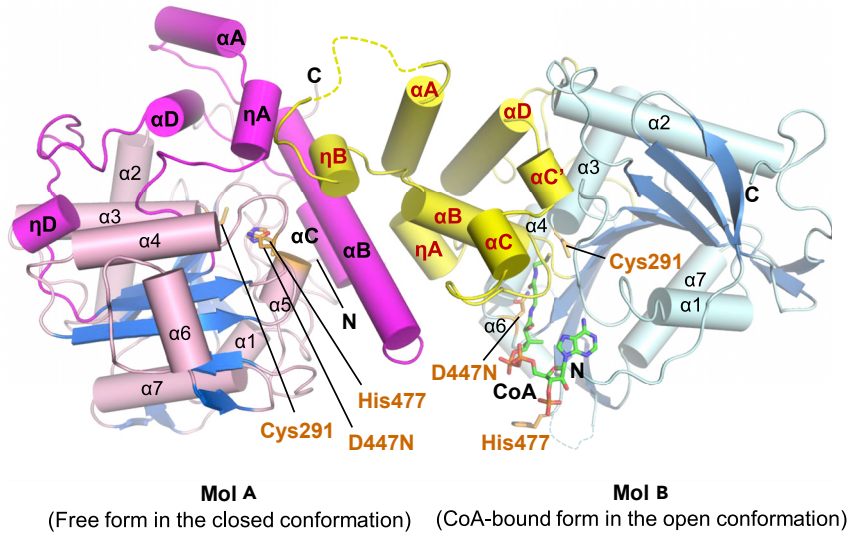

Figure 2. Structure of the PhaC$_{Cs}$-CAT Heterodimer Formed by the Free and CoA-Bound Forms

The CoA-PhaC$_{Cs}$-CAT complex contains the free form in the closed conformation (pink and magenta) and the CoA-bound form in the open conformation (cyan and yellow). The dimer interface is composed of CAP subdomains (magenta and yellow) from each protomer. The bound CoA is shown as a green stick model. Basically, PhaC$_{Cs}$-CAT comprises the α/β core subdomain formed by α-helices (α1–α7), β-strands (β1–β12), and 3$_{10}$-helix (η1) with the CAP subdomain formed by α-helices (αA–αD) and 3$_{10}$-helices (ηA–ηD). Compared with the free form, the CoA-bound form lacks η1, η2, and α5 in the α/β core and long αB and ηD in the CAP subdomains.

The Free Form of PhaC$_{Cs}$-CAT in the Closed Conformation

The free form (Mol A) in the current structure displays the α/β core subdomain (residues 186–318 and residues 439–561) and comprises the central parallel and antiparallel mixed β-sheet (β1–β12) with α-helices (α1–α7) located at both sides of the central β-sheet (Figure S3). The CAP subdomain is formed by 120 residues (residues 319–438), which is inserted between β7 and β8 strands and topologically projected from the α/β core subdomain (Figure S3). The free form displays an ordered helical CAP subdomain, which comprises four α-helices (αA-αD) and two 3$_{10}$-helices (ηA and ηD) in the sequence ηA-αA-αB-αC-αD-ηD and makes intimate contacts with the α/β core subdomain (Figure 3A). The CAP subdomain is characterized by the presence of a long αB helix comprising 26 residues (Gly354-Leu379) and consists of a prominent antiparallel helix bundle formed by long αB and short αC helices and another antiparallel helix bundle formed by αA and αD helices (Figure 3B). Notably, the long αB helix is kinked at Thr360 because of interference of the regular main chain-main chain hydrogen bonds of the helix by the side chains of Thr360 and Ser363 residues, which form hydrogen bonds with main-chain amide groups of the helix (Figures 3B and S4). The LID region (Pro327-Pro386) forms the ηA-αA-αB segment in an ordered structure. Importantly, the segment of αB helix, αB-αD loop, and αD helix completely covers the active site containing Cys291, Asp447, and His477 located at the bottom of the cavity (Figures 3A and 3B). This tightly closed conformation is comparable to the closed conformation of the free form of a previously reported PhaC$_{Cs}$-CAT symmetrical homodimer (Chek et al., 2017). Structural overlay of these two free forms shows that the free form of PhaC$_{Cs}$-CAT in the symmetrical homodimer exhibits unfolding of part of the LID region, the C-terminal part (Phe361-Leu379) of αB helix into a short 3$_{10}$-helix (ηB) and a long loop encompassing the disordered region (Tyr373-Thr383), resulting in an incomplete closed conformation (Figures 3C and S3). As discussed later, the closed conformation of the free form in the current heterodimer is stabilized by intimate contacts with the CAP subdomain from the CoA-bound form. The free form in the symmetrical homodimer possesses no such interactions, and therefore the CAP subdomain is in a metastable state, which contains a disordered LID region (Chek et al., 2017).

The CoA-Bound Form of PhaC$_{Cs}$-CAT in the Open Conformation

The CoA-bound form (Mol B) displays unexpected global conformational changes in the CAP subdomain and additional local changes in the α/β core subdomain. Three segments display poor electron density, suggesting conformational disorder: part (Ala347-Lys355) of αA-αB loop in the CAP subdomain, β9-β10

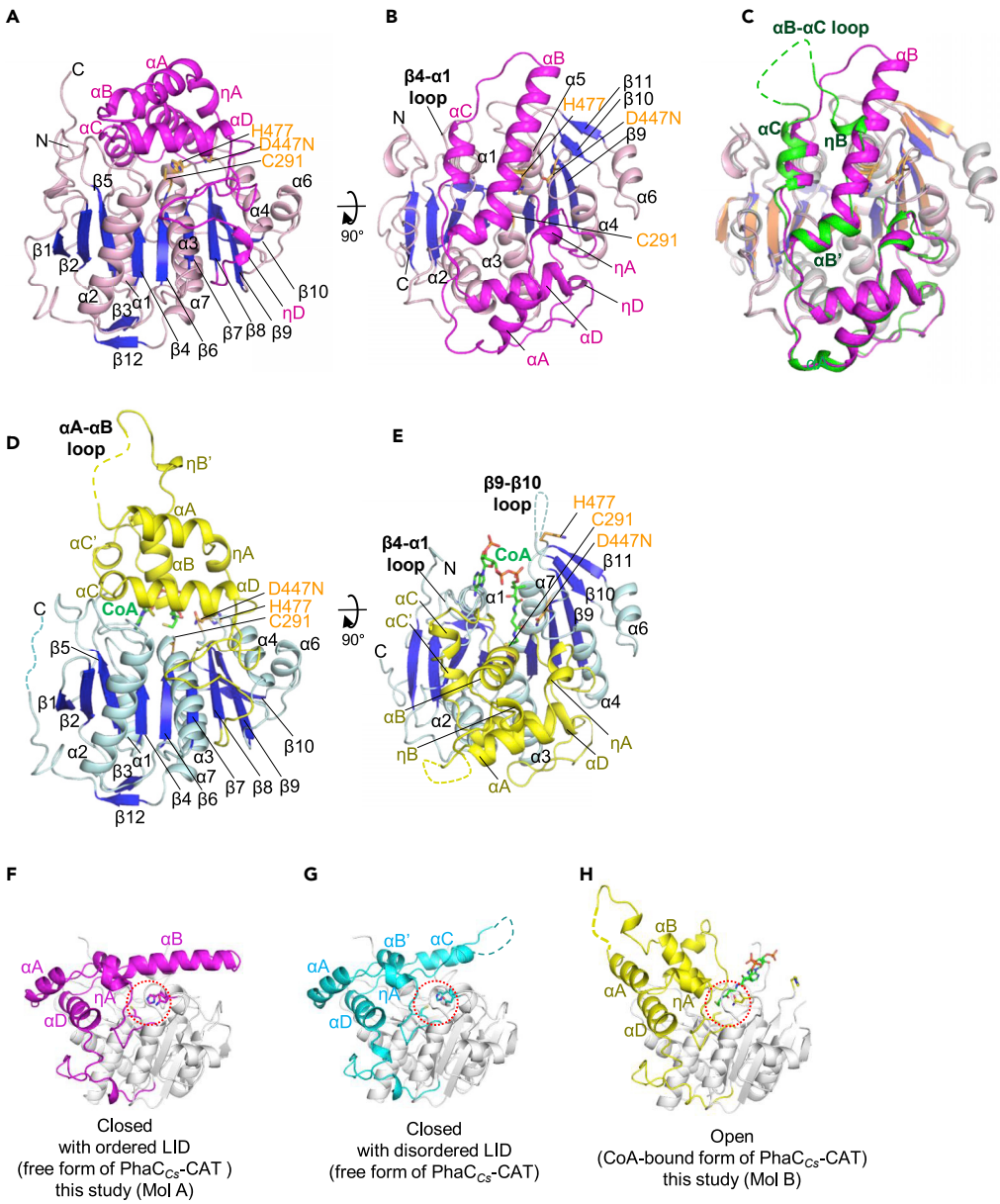

Figure 3. The Free and CoA-Bound PhaC$_{Cs}$-CAT Structures Found in the Heterodimer

(A) Side view of the free form (Mol A) of the PhaC$_{Cs}$-CAT heterodimer. The free form contains the α/β core (pink with blue for β-strands) and CAP (magenta) subdomains. Catalytic triad residues Cys291 (C291), His477 (H477), and Asn447 replacing Asp447 (D447N) are shown as stick models (orange).

(B) As in (A), but a top view down to the active site cleft.

(C) As in (B), but superimposed with the free form of PhaC$_{Cs}$-CAT homodimer (PDB 5XAV) with the α/β core subdomain in gray, β-strands in orange, and the CAP subdomain in green. The LID region of the CAP subdomain forms short α- and 3_{10}-helices (αB and ηB, respectively) with a disordered region (shown as broken lines).

(D) Side view of the CoA-bound form (Mol B) of the PhaC$_{Cs}$-CAT heterodimer. The free form contains the α/β core (cyan with blue β-strands) and CAP (yellow) subdomains. Catalytic triad residues are shown as in (A). Part (residues 347–355) of αA-αB loop and the C-terminal region (residues 548–567) are disordered and shown as broken lines.

(E) As in (D), but top view down to the active site cleft. The disordered region (Ile478-Asp488) of β9-β10 loop is shown as a broken line.

(F) Side view of the free form of PhaC$_{Cs}$-CAT in the heterodimer (this study). The CAP subdomain (magenta) displays the closed conformation with long αB helix of the LID region. The active site is marked with a red broken-line circle.

Figure 3. *Continued*
(G) As in (F), but for the free form of PhaC$_{Cs}$-CAT in the homodimer (PDB 5XAV). The CAP subdomain (cyan) displays another closed conformation with a disordered region by unfolding of αB helix.
(H) As in (F), but for the CoA-bound form of PhaC$_{Cs}$-CAT in the homodimer (this study). The CAP subdomain (yellow) displays an open conformation with dynamic conformational rearrangement of the LID region and a large positional shift away from the active site.

loop (Ile478-Asp488), and the C-terminal end region (Pro548-Asn567) in the α/β core subdomain (Figures 3D and 3E). The conformational changes in the CAP subdomain comprise unfolding of the N-terminal half of αB helix into a disordered region and a loop containing a short 3_{10}-helix (ηB), reorientation of αA helix, a positional shift of αB helix, and a split of αC helix into short αC and αC′ helices with a large positional shift. These conformational changes uncover the active site and allow for entry of the CoA molecule into the active site cleft (compare Figures 3B–3E).

These conformational changes accompany local conformational changes in the α/β core subdomain. The conformational changes in αC-αD loop induce disordering of the C-terminal end region of the α/β core subdomain (Figure 3B). In the closed conformation, αB helix stabilizes the β9-β10 loop by making direct contacts. In the open conformation, removal of αB helix from the active site induces disordering of β9-β10 loop and is accompanied by unfolding of α5 helix, resulting in a large positional shift of catalytic triad residue His447 away from the active site toward the outside of the cleft (compare Figures 3B–3E). Therefore, the catalytic Cys-His-Asp triad is lost in the open conformation, which will be further discussed later. Similarly, removal of αC helix from the active site induces refolding of β4-α1 loop.

In summary, our structure, together with previous structures of the free forms, clarified the dynamic properties of the CAP subdomain with a series of conformational changes (Figures 3F–3H). The free form of PhaC$_{Cs}$-CAT in the current heterodimer displays a tightly closed conformation with the ordered CAP subdomain (Figure 3F), which bears a close resemblance to the partly closed conformation of the free form of PhaC$_{Cs}$-CAT in the symmetric homodimer (Figure 3G). The CoA-bound form of PhaC$_{Cs}$-CAT in the current asymmetric heterodimer elucidates the open conformation by unexpectedly large conformational changes to incorporate CoA into the active site cleft (Figure 3H). The conformational changes in the CAP subdomain mediate local conformational changes in the α/β core subdomain, suggesting a key role in the catalytic activity of PhaC.

Interface between the Free and CoA-Bound Forms in the PhaC$_{Cs}$-CAT Heterodimer

At the dimer interface, direct contacts between the CAP subdomains from the free and CoA-bound PhaC$_{Cs}$-CAT protomers bury a large total accessible surface area (ASA) of 1,922 Å^2. The LID regions of the CAP subdomains from both PhaC$_{Cs}$-CAT protomers participate in intimate intermolecular contacts at the dimer interface. Nonpolar residues located at the molecular surface of αB helix of the free form represent the core of the interface composed of ηA helix, αB helix, the loop between αB and αC helices, αB-αC loop, and αC helix from the free form (Figure 4). These nonpolar residues contact with ηA helix, ηB helix, αB helix, and αB-αC loop from the CoA-bound form. Notably, Trp371 of the free form (Mol A), Trp371(A), is located at the αB helix and exposed to the outside. This unusually exposed nonpolar aromatic residue is sandwiched between Phe361 and Leu369 from the CoA-bound form (Mol B), Phe361(B) and Leu369(B) (Figure 4A).

In addition to these hydrophobic interactions, intermolecular polar interactions also contribute to the dimer interface. Among these, Asn367, a conserved residue in Classes I and II, plays a key role in the polar interactions. Asn367(A) of the free form is located at αB helix and forms hydrogen bonds with Arg365(B) and the main chain of ηB helix of the CoA-bound form (Figure 4A). Asn367(B) of the CoA-bound form does not participate in intermolecular interactions but comprises the N-terminal cap of αB helix and forms intramolecular hydrogen bonds with the flanking loop (the main chains of Leu364(B), Arg365(B), Asp368(B), and Leu369(B)). These interactions seem to be important for maintaining the conformation of the N-flanking region of αB helix for intermolecular interactions.

Glu329 located at ηA helix is another key residue in the intermolecular polar interactions (Figure 4A). Glu329(A) of the free form forms hydrogen bonds with Thr360(B) and its main chain and Ser363(B) from ηB helix of the CoA-bound form. Glu329(B) of the CoA-bound form forms a hydrogen bond with the main chain of Ala385(A) of the free form. Glu329 is a non-conserved residue (Figure S3), which may contribute to the high activity of PhaC$_{Cs}$.

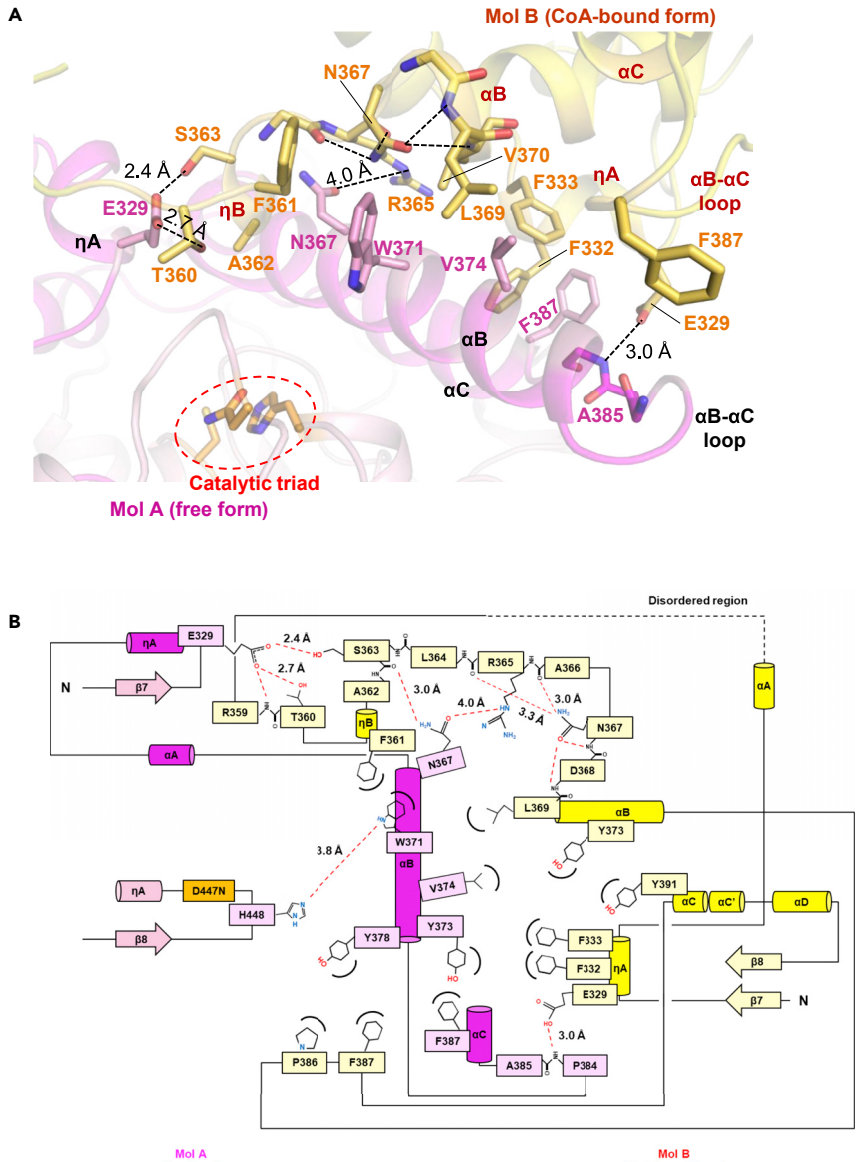

Figure 4. The Dimer Interface of the Free and CoA-bound PhaC$_{Cs}$-CAT Heterodimer

(A) A close-up view of the dimer interface of the free and CoA-bound PhaC$_{Cs}$-CAT heterodimer. At the direct contact region of the CAP subdomains from the free (Mol A in magenta) and CoA-bound (Mol B in yellow) forms, the side chains of residues involved in the contacts are shown as stick models. The nonpolar contact areas comprise αB helix (Trp371 and Val374) and αC helix (Phe387) from the free form (magenta), contacting with ηA helix (Phe332, Phe333), ηB helix (Phe361, Ala362), αB helix (Leu369, Val370), and αB-αC loop (Phe387) from the CoA-bound form (yellow). The intermolecular polar interactions comprise ηA helix (Glu329), αB helix (Asn367), αB-αC loop (Ala385 main chain) from the free form to interact with ηB helix (Ser363, Thr360) and αB helix (Asn367, Arg365) and ηA helix (Glu329) from the CoA-bound form.

(B) A schematic summary of intermolecular interactions between the free and CoA-bound forms of PhaC$_{Cs}$-CAT forming the asymmetric heterodimer. Hydrogen bonds are shown as broken lines.

CoA Molecule Bound to PhaC$_{Cs}$-CAT

The CoA molecule consists of an ADP-3′-phosphate moiety and a pantetheine arm, which is formed by a pantothenate and a terminal β-mercaptoethanolamine (Figures 1B and 5A). We found clear electron density of CoA bound to the active site of PhaC$_{Cs}$-CAT (Mol B) in the open conformation (Figure 5A). The active site cleft is created between the CAP and α/β subdomains and comprises β4-α1 loop, β8-α4 loop containing Asn447 (Asp447 in the wild-type), and β9-β10 loop containing His477 from the α/β core subdomain and

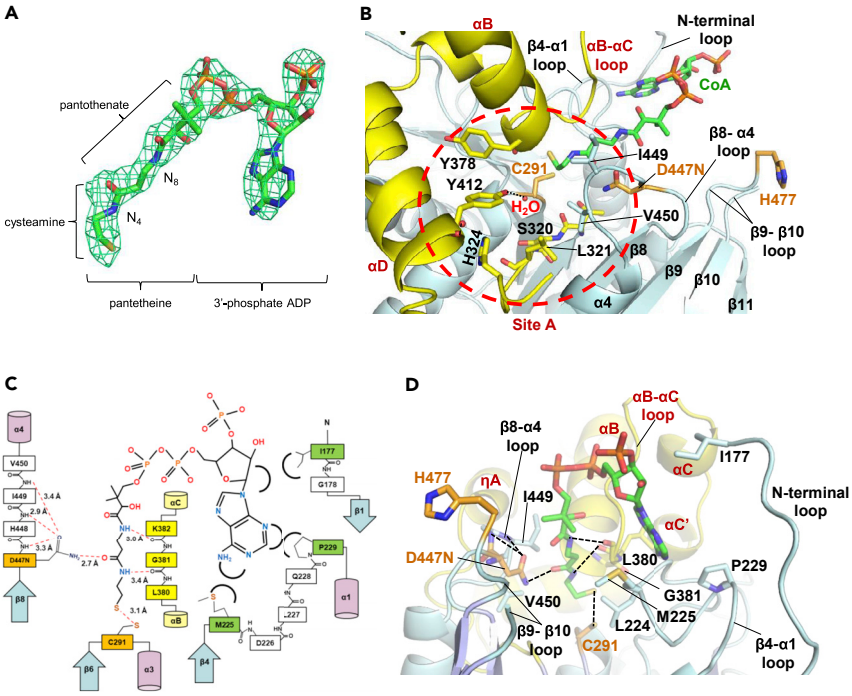

Figure 5. Coenzyme A (CoA) Bound to PhaC$_{Cs}$-CAT in the Open Conformation

(A) Model of CoA in the omit electron density map (F_o-F_c) at a contour level of 3σ. The CoA molecule consists of a pantetheine arm and a 3′-phosphate ADP moiety.

(B) Side view of the opened active site cleft. The pantetheine arm of CoA (green) is extended into the active center. The cleft is formed by the CAP (yellow) and α/β core (cyan) subdomains. A conserved water molecule (red dot) was observed in the possible pocket Site A and forms a hydrogen bond (3.5 Å) with Y412. In this figure, other hydrogen bonds are not shown for clarity. His477is shifted by ~22 Å away from Cys291.

(C) Schematic summary of the intermolecular interactions between PhaC$_{Cs}$-CAT and CoA. Catalytic residues (orange), residues from the CAP subdomain (yellow), and hydrophobic residues binding the adenine group (green) are shown.

(D) CoA (stick model in green) bound to PhaC$_{Cs}$-CAT. The α/β core subdomain (cyan) and CAP subdomain (yellow) are shown. The catalytic residues, Cys291, and the replaced Asn447 (D447N) directly interact with CoA to form hydrogen bonds. Main-chain oxygen atoms from Leu380 and Gly381 form hydrogen bonds with CoA amide groups (N_4 and N_8). Hydrogen bond distances are given in (C).

αB-αC loop from the CAP subdomain (Figure 5B). The ADP moiety of CoA is located at the entrance of the active site cleft and the extended pantetheine arm of CoA is inserted into the active site so as to position the terminal thiol (SH) group of cysteamine at the active center close to Cys291. The intermolecular interactions between CoA and PhaC$_{Cs}$-CAT contain both hydrogen bonds and nonpolar contacts involving both the ADP and pantetheine moieties of CoA with PhaC$_{Cs}$-CAT residues from both the CAP and α/β core subdomains (Figure 5C). The sulfur atom (S_1) of the terminal SH group of CoA is located at a distance of 3.1 Å from the catalytic center Cys291 (S_γ) (Figure 5D). The distance is shorter than the typical SH—S hydrogen bond distance (3.9 Å) and also longer than a disulfide bond with S-S distance ~2.1 Å, suggesting a mixture of the SH—S hydrogen bond and the S-S bond in an oxidized state.

The cleft is mostly hydrophobic with nonpolar residues (Leu224, Met225, Ile449, Val450) from both the α/β core subdomain, whereas the main chain (Leu379, Leu380, Gly381) of αB-αC loop from the CAP subdomain provides polar interactions with CoA. The pantetheine arm of CoA is locked by forming hydrogen bonds with the main-chain carbonyl groups of Leu380 and Gly381 from αB-αC loop (Figure 5D). The side chain of mutated Asn447 also forms a hydrogen bond with the pantetheine arm of CoA. The adenine moiety of CoA fits into a hydrophobic cavity derived from Met225 and Pro229 from β4-α1 loop, and the ribose ring is covered by nonpolar residues (Ile177) from the extended N-terminal loop. The corresponding residues are highly conserved in hydrophobicity among classes I and II PHA synthases (Figure S3). Our observed interactions between CoA and the active site cleft of PhaC$_{Cs}$-CAT are consistent with results in previous studies indicating the importance of the CoA

moiety in substrate binding for PhaC catalytic activity (Gerngross and Martin, 1995; Ushimaru et al., 2013; Zhang et al., 2015).

Active Site of the PhaC$_{Cs}$-CAT Heterodimer

PhaC possesses a conserved catalytic triad comprising Cys, Asp, and His residues, which are important for its catalytic activity. The geometry of the triad shows a sharply distinct difference between the free and CoA-bound forms (Figure S5A). The geometry of the triad of the current free form displays similarity to that of the free form in the homodimer (Chek et al., 2017) (Figure S5B and S5C). Cys291 and Asn447 (Asp447 in the wild-type) of the CoA-bound form are well overlapped with those of the free form, although His477 of the CoA-bound form is unexpectedly shifted out from the catalytic pocket by the unfolding of β9-β10 loop containing short α5 helix. The conformational shift of β9-β10 loop is essential for CoA binding to create a cleft for the terminal cysteamine moiety of the bound CoA molecule to be inserted into the active center. His477 was proposed to activate Cys291, by accelerating deprotonation of the Cys thiol group without participating in the PHA elongation process (Stubbe and Tian, 2003). The His477 movement out from the active site without disruption of the arrangement of the other active residues suggests that this asymmetric heterodimer structure may mimic an elongation state in PHA biosynthesis. This movement of His477 out of the catalytic pocket supports the proposed mechanism wherein the His477 is only required for the initiation stage. Another catalytic residue, Asp447, was proposed to act on the PHA elongation process by attacking the hydroxyl group in the acyl moiety of the acyl-CoA substrate. In our CoA-bound form, hydrogen bonds between the side chain of Asn447 and the carbonyl group (O_5) of CoA were observed (Figure 5D). This interaction is consistent with previous report that a D480N mutation in $(His)_6$-tagged PhaC$_{Cn}$ decreased the reaction rate to 0.0008 units/mg from 20 unit/mg observed in wild-type (Tian et al., 2005).

We previously proposed Site A or Site B as the potential binding pocket for the acyl moiety of the substrate acyl-CoA molecule (Chek et al., 2017). In the current CoA-bound form, Site A consists of Ser320, Leu321 and His324 (from β7-αA loop), Tyr412 (αD helix), and Ile449 and Val450 (β8-α4 loop), as found in the free form (Figure 5B). In addition to these residues, Tyr378 from shifted αB helix also participates in forming Site A of the CoA-bound form. A water molecule, which may mimic the hydroxyl group of the 3HB acyl group, was found at a distance close enough to interact with the hydroxyl group of Tyr412. This observation suggests that Site A seems to be the most probable binding pocket for the acyl moiety from acyl-CoA. Contrary to Site A showing conservation of residues forming the site, Site B is modified by conformational changes in β4-α1 loop and the polar residue Asn220 in Site B is flipped out from the cavity.

The Open-Closed Conformational Transition

To understand the dynamic transition from the closed to the open conformations, the structures of the free and CoA-bound forms of PhaC$_{Cs}$-CAT were compared (Figures 6A and 6B). The movement from closed to open conformational changes of PhaC$_{Cs}$-CAT is also shown in Video S1. The restructured region in the CAP subdomain is not only limited to the LID region (residues Pro327–Pro386) encompassing αA and αB helices but also includes αC helix (Phe387-Asn394) (Figure S3). The major conformational and positional transition in the CAP subdomain is observed at αB and αC helices, which are responsible for blocking substrate entry in the closed conformation, suggesting that both αB and αC helices form a lid that should be open for substrate entry (Figure 6C). Large movements of αB and αC helices accompany partial unfolding of both helices with a split of αB into shorter ηB and αB helices and a split of αC into shorter αC′ and αC helices. The movement of helices αB and αC resembles a retracting "Boom gate" mechanism, which covers the active site and blocks substrate entry. This large movement is also accompanied by reorientation of ηA and αA helices, whereas αD helix does not undergo conformational or positional changes.

The dynamic conformational transition of the CAP subdomain induces local conformational changes in loops of the α/β core subdomain. The most striking conformational rearrangement is found in β9-β10 loop induced by removal of αB helix as mentioned above (Figure 6D). Moreover, partial unfolding of αC helix induces refolding of β4-α1 loop to enable Met225 and Pro229 to form a nonpolar pocket for binding to the CoA adenine ring, which stacks onto the Met side chain (Figure 6E). In the closed conformation, the N-terminal loop is also stabilized by αC helix of the CAP subdomain. In the open conformation, αC helix is moved away from the N-terminal loop. Then, the N-terminal loop is shifted to interact with CoA by stacking Ile177 on the ribose ring of CoA (Figure 6F). Thus, the open-closed conformational transition is accomplished by concerted movement of the CAP subdomain and a set of loops of the α/β core subdomain.

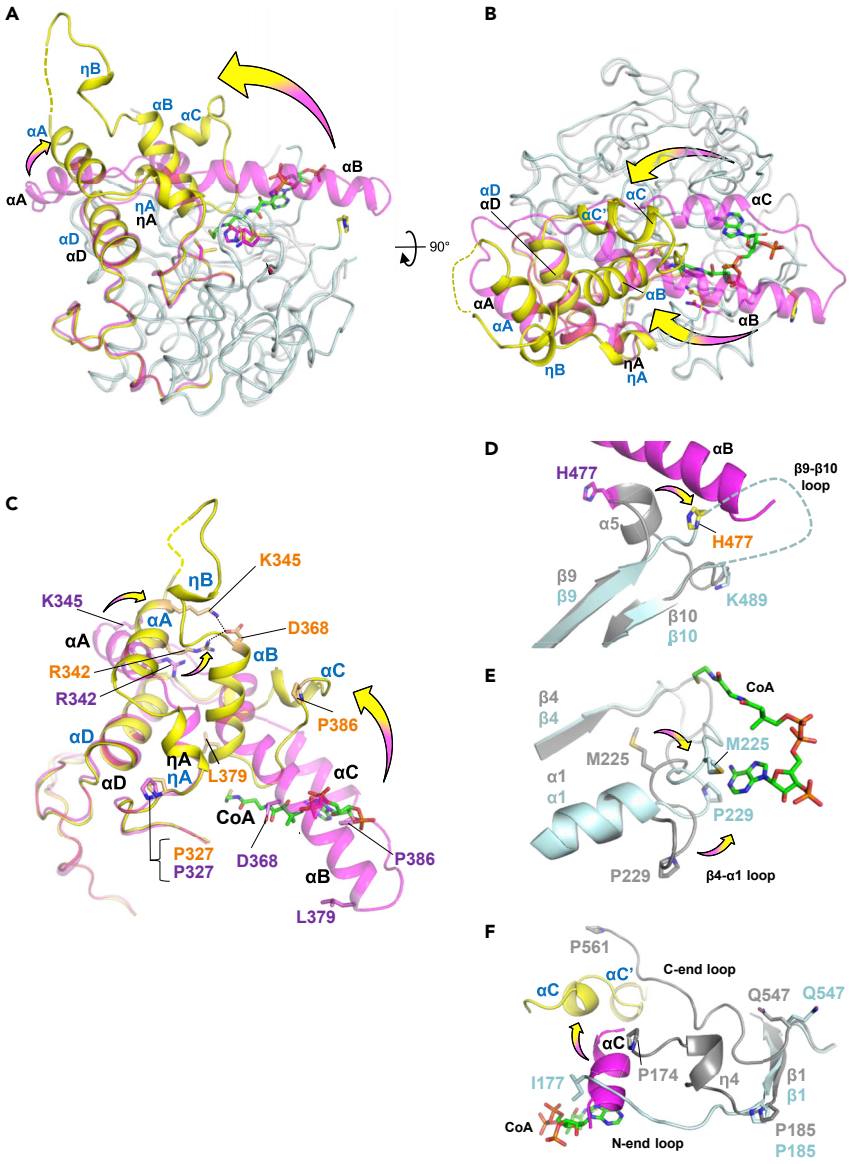

Figure 6. Dynamic Conformational Changes at CAP Subdomain Regulate Closed-Open Form for Substrate Entry

(A) Overlay structures of fully closed and open form of $PhaC_{Cs}$-CAT (D447N). The α/β core subdomain (gray in closed form; cyan in open form) displays high similarity, whereas the CAP subdomain (magenta in closed form; yellow in open form) undergoes significant conformational changes to allow substrate entry. Coenzyme A is shown in stick form (atom color codes are green for C, blue for N, red for O, orange for P, and yellow for S).

(B) As in (A), but a top view down to the active site.

(C) The LID region (P327-P386) is completely restructured with the first helix movement being observed at R342 and K345, which appear to be interacting with D368 in the open form. In the closed form, a long helix αB consisting of D368-L379 covers the catalytic pocket. The residue P386 also moves in. The fully closed (magenta) and fully open (yellow) forms are shown.

(D) In the closed form, αB helix (magenta) stabilizes α5 helix (gray) by direct contacts. In the open form, removal of αB helix induces unfolding of α5 helix and β9-β10 loop and results in shifting the His477 (magenta in closed form; yellow in open form) out from the catalytic pocket.

(E) Refolding of β4-α1 loop in the open conformation enables CoA binding by repositioning Met225 and Pro229 (cyan) to form a nonpolar binding pocket for binding to the CoA adenine ring.

(F) The N-terminal end loop (gray) is stabilized by αC helix (magenta) in the closed conformation. In the open conformation, αC helix splits into short αC and αC′ helices (yellow) with a large positional shift, which induces a conformational change of the N-terminal end loop (cyan) to interact with the bound CoA (green sticks) with Ile177. The C-terminal end loop (Pro548-Pro561) is disordered in the open conformation.

Key Residues Supporting the Conformationally Dynamic Properties of the CAP Subdomain

Based on structural comparison of each segment of the CAP subdomain, we sought to identify key residues that mediate the CAP conformational transition (Figure 7). αA helix packed on αD helix displays remarkable reorientation against αD helix on the open-closed transition. At the interface between αA and αD helices, Arg409 of αD helix forms salt bridges with both Glu336 and Glu343 from αA helix (Figure 7A). These three residues are conserved in class I PhaC. The reorientation of αA helix was accompanied by a flip of the side chain of Arg409, while maintaining salt bridges with Glu336 and Glu343 (Figure 7B). Thus, reorientation of αA helix acts as a hinge to induce a large movement of αB and αC helices. A mutation (R409A) of the key residue Arg409 significantly reduced PhaC activity using 3HB-CoA as a substrate, suggesting that the conformational transition is essential for the activity (Figure 7I).

The extended helix αB is the main part of the lid blocking substrate entry and displays dynamic conformational changes. In the closed conformation, Arg365 and Asp368 from αB helix are positioned in the active site pocket and form hydrogen bonds with His448, Cys291, and His477 (Figure 7C). These hydrogen bonds should be key interactions in maintaining αB helix as a lid of the active site in the closed conformation. Interestingly, in the open conformation, both Arg365 and Asp368 contribute to stabilize partly unfolded αB helix by interacting with Asp335 (αA-ηA loop) and both Arg342 and Lys345 (αA helix), respectively (Figure 7D). The dynamic αB helix movement creates a cleft at the molecular surface for CoA entry. Alanine mutation of Arg365 (R365A) and Asp368 (D368A) abolished or significantly reduced catalytic activity (Figure 7I). It is possible that the formation of bifurcated hydrogen bonds and a salt bridge between Arg365 and Asp355 effectively contributes to stabilization of shifted αB helix in the open conformation.

In the closed conformation, αC helix is required to completely cover the active site, together with long αB helix. This helix is stabilized by Asp388 and Asp395 by forming a hydrogen bond with Asn231 and a salt bridge with Lys221, respectively (Figure 7E). With the open-closed transition, αC helix (Phe387-Asn394 in the closed form) is divided into two shorter helices, αC (Leu389-Trp392) and αC′ (Asp395-Asp398) helices, in the open form (Figure 7F). The hydrogen bond between Asp388 and Asn231 and the salt bridge between Asp395 and Lys221 are broken in the transition, whereas Asp395 switches to form a hydrogen bond to the main chain of Lys221 and stabilizes reoriented αC and αC′ helices in the open conformation. In the open-closed transition, αC-αD loop containing Asp395 acts as a second hinge, with αA helix as the other hinge, which is reoriented against αD helix.

Another important rearrangement of interactions is found with Asp398 (αC-αD loop), which forms a hydrogen bond to the main chain (Met559) of the C-terminal end loop in the closed form (Figure 7G). In the open form, Asp398 forms a hydrogen bond with Asn393 in the same loop so as to pack αC and αC′ helices in a compact form, thereby creating space for CoA entry (Figure 7H). As shown in Figure 4A, Ser363 of the CoA-bound form contributes to stabilization of the open conformation by forming an intermolecular hydrogen bond with Glu329 from the free form. Alanine mutation (S363A) of this residue reduced catalytic activity by prolonging the lag phase (Figure 7I).

To investigate mutational effects of key residues on PHA content and substrate specificity, we performed *in vivo* PHA biosynthesis assays using crude palm kernel oil as carbon source (Figure S6). All four mutants, S363A, R365A, D368A, and R409A were able to accumulate similar PHA content as the wild-type (Figure S6A). PHA copolymers such as [P(3HB-*co*-3HHx)] copolymer with relatively higher 3HHx composition are great candidates for industrial usages, so it would be informative to observe the changes of 3HHx fractions in the PHA synthesized by the mutants. In contrast to the *in vitro* enzyme assay, the R365A mutant is capable of synthesizing PHA, but failed to incorporate 3HHx monomers with only 0.2 mol % 3HHx fraction, when compared with that of the wild-type (3.1 mol%) (Figure S6B). This contradicting result indicates that the R365A mutant is still capable of synthesizing PHA in the *in vivo* system, where the cultivation period (2 days) is longer than the *in vitro* activity assay (5 mins). To our surprise, one mutant, D368A was able to incorporate slightly more 3HHx fractions (3.9 mol %) than the wild-type (Figure S6B). The mutations to alanine disrupt the stability of both closed and open conformations; further examination of mutations to other amino acids may provide clearer results. Nevertheless, these results have shown that the LID region is highly important for PhaC activities and that the mutations will strongly affect the performances and substrate specificities of the enzymes.

Product Egress Path

The active center residue Cys291 faces Site A, which is the potential binding pocket for the acyl moiety of the bound substrate acyl-CoA molecule (Figure 5B). Our model building study suggested that Site A

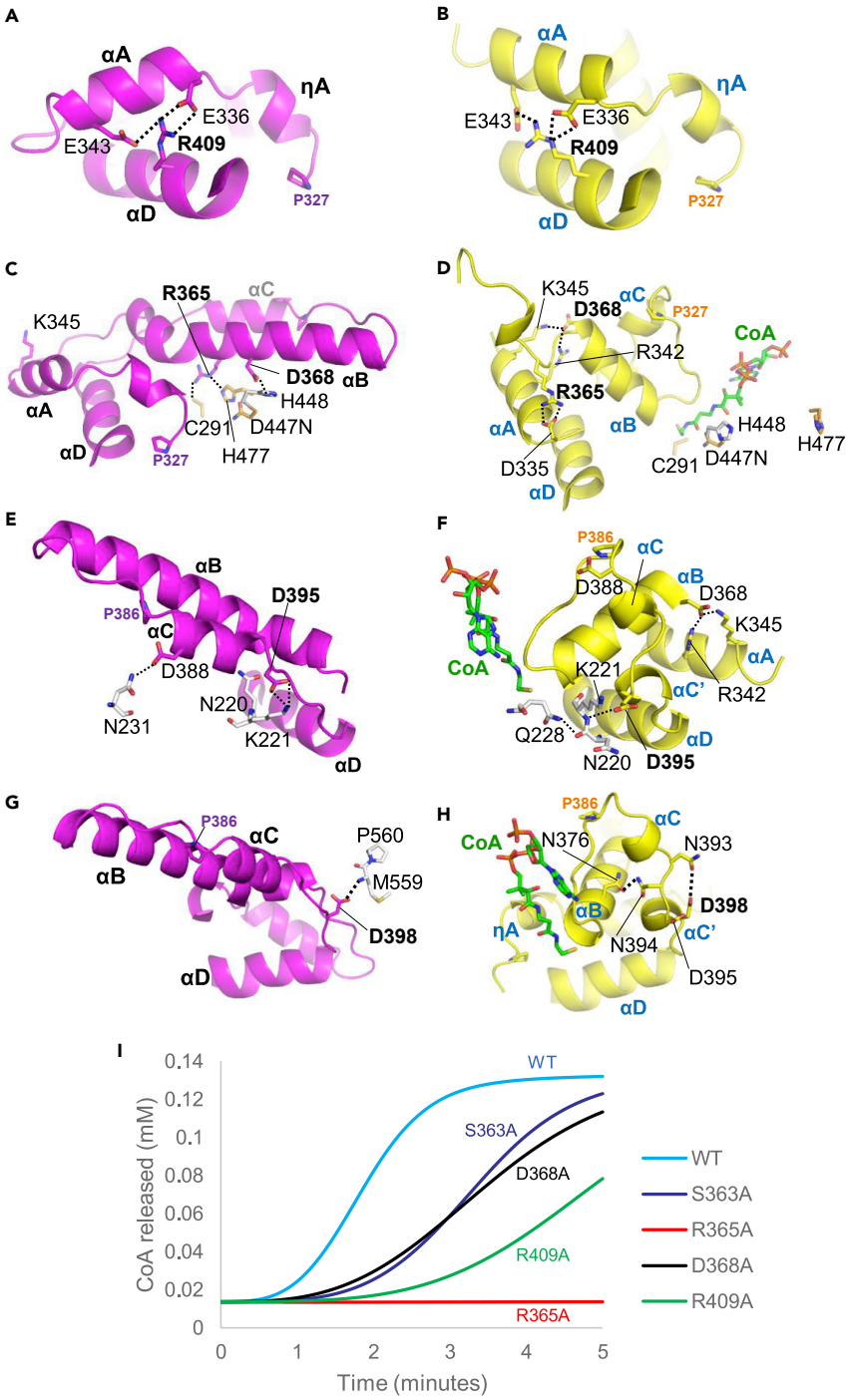

Figure 7. Helices αB and αC Are Key in the Open-Closed Conformational Change

(A–H) (A), (C), (E), and (G) show LID segments of the CAP subdomain from the closed (magenta) conformation of $PhaC_{Cs}$-CAT and (B), (D), (F), and (H) show open (yellow) conformation. Residues from the α/β core domain are depicted in gray. For visualization, αD helices from both closed and open conformations were aligned. (A and B) The first hinge residue R409 interacts with E336 and E343 to effect tilting up of αA helix. (C and D) R365 and D368 hold αB helix closer to the catalytic triad in the closed form and retract αB helix in the open form. (E and F) The second hinge D395 interacts with K221. In the open form, D388 is free from interaction with N231 and contributes to the opening. (G and H) D398 contributes to lift up αC helix in the open form, to effect opening of the substrate entry pathway by dividing αC helix. (I) Enzymatic activity of PhaC with 3HB-CoA substrate. Significant effects were observed for mutations on non-catalytic residues that may contribute to the open-closed conformational transition.

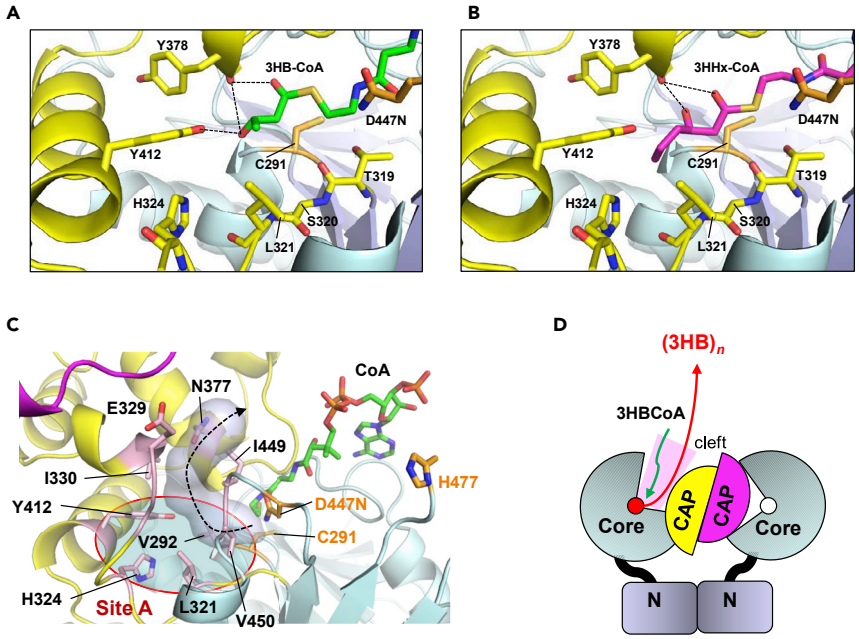

Figure 8. Models of Acyl-Coenzyme A in the Active Pocket

(A) 3HB-CoA (four carbons) were modeled to fit in the binding pocket. The thioester group of 3HBCoA was positioned close to the catalytic Cys291. Site A of the active site could accommodate the 3HB moiety, with stabilization by formation of hydrogen bonds (dashed lines) with the hydroxyl group of Tyr412 and the main chain of Tyr378.

(B) As in (A) but for 3HHx-CoA (6 carbons) as a ligand. Site A has the capacity to accommodate the longer acyl chain of 3HHx-CoA.

(C) A potential tunnel utilized for product egress (gray surface with dashed arrow) from Site A (red circle) of the active site. The tunnel is part of the large cleft that allows entry of acyl-CoA substrate.

(D) An alternative model for the substrate entry and product release mechanism through a large cleft (pink) created in the open form molecule (yellow CAP), which is stabilized by the closed form molecule (magenta CAP) in an asymmetric dimer. The N domain is proposed to contribute to stabilization of the dimer.

accommodates the acyl groups from the substrate such as 3HB-CoA and 3HHx-CoA (Figures 8A and 8B). In these models, the 3-hydroxyl group of each acyl group is located at a position close to the position of the bound water molecule found in the crystal structure (Figure 5B) and could be stabilized by polar interactions with the side-chain hydroxyphenyl group from Tyr412 and the main chain of Tyr378. The mutation of Tyr445 (corresponding to Tyr412 in PhaC$_{Cs}$) to Phe in PhaC of *Cupriavidus necator* (PhaC$_{Cn}$) was reported to affect its substrate specificity, further supporting the importance of Tyr412 in substrate recognition (Rehm et al., 2002).

Modeling also suggested that the acyl group of the substrate, which is covalently bound to Cys291 is located at Site A. These results are consistent with our structural investigation in search of a possible egress tunnel/channel of the product PHA chain using the program CAVER, a software tool for analysis and visualization of tunnels and channels in protein structures (Chovancova et al., 2012) (Figure 8C). The egress path, which is ~22.1 Å in length, is formed by helices and loops from the CAP subdomain (the C-terminal end of αB helix, and the following αB-αC loop, β7-ηA loop, and ηA helix) and β8-α4 loop from the CAT subdomain. The narrowest distance in the tunnel is ~2 Å in diameter and is capable of accommodating the (3HB)$_n$ polymer chain. Site A contains polar residues (Tyr412 and His324), whereas the egress path comprises mostly hydrophobic and nonpolar residues (Val292 from α3 helix, Ile330 from ηA helix, Ile449, Leu321 from β7-ηA loop, and Val450 from β8-α4 loop). Our analyses showed that the active site cleft accommodating the CoA molecule also possesses additional space to accommodate a product PHA chain from Site A, suggesting that the cleft is capable of playing a role in accommodating both substrate and product simultaneously, with the hydrophobic Ile449 as the center point in separating CoA and the putative egress (Figure 8C). The cleft connecting CoA, Site A, and the putative egress pathway has provided an alternative mechanism for understanding the polymerization of PHA (Figurea 8D and S7).

DISCUSSION

We have determined the complex structure of PhaC$_{Cs}$-CAT with CoA. The structure adopts an asymmetric dimer comprising two protomers in different forms, a CoA-free form in the closed conformation and a CoA-bound form in the open conformation to accommodate the CoA molecule in the active site cleft created by dynamic conformational transition in the CAP subdomain and local conformational shifts in the α/β core subdomain. The dimer interface comprises the CAP subdomains from the two protomers and reveals that the CAP subdomain from the closed conformation stabilizes the CAP subdomain in the open conformation through intimate direct interactions. The observed stabilization of the CoA-bound open conformation by the other protomer of the dimer could account for the fact that the dimer form of PhaC is essential for enzymatic activity. The current structure also leads us to speculate that the conformational changes from the homodimer to this asymmetric heterodimer may cause the lag phase observed in most Class I PhaCs. Previous studies have reported that the trimeric CoA analog has reduced the lag phase and shifted most PhaC$_{Cn}$ to dimer formations (Wodzinska et al., 1996). Our asymmetric dimer is in agreement with the observation, where the trimeric acyl group may occupy the egress pathway and stabilize the open-closed dimer conformation of PhaC. In the same study, the radiolabeled non-hydrolyzable trimer substrates were bound to dimer with a stoichiometry of approximately 1 radiolabel per PhaC$_{Cn}$ dimer (Wodzinska et al., 1996). Our current asymmetric dimer bound to a CoA molecule fits the observation of the 1 substrate to 1 dimer ratio.

The CAP subdomain in the free form dimer of PhaC$_{Cs}$-CAT (Chek et al., 2017) displays a disordered region at the LID region. This disordered region is folded into short αB helix in the open conformation and forms a compact αB-αC-αC′ segment that directly interacts with CoA (Figures 5B–5D). This interaction suggests that this flexible region could play a role in CoA sensing and act as a trigger for dynamic conformational changes in the CAP subdomain for full binding of CoA to the active site.

Previously, two catalytic mechanisms were proposed in the context of biochemical observations of an enzymatically active dimeric form of PhaC (Stubbe et al., 2005). One mechanism comprised a *non-processive ping-pong model* that required two sets of active sites for PHA chain elongation with chain transfer between the two Cys residues at the active centers of dimerized protomers across the dimer interface (Gerngross et al., 1994; Griebel et al., 1968; Kawaguchi and Doi, 1992). The other mechanism involved a *processive model* that requires a single active site for PHA chain elongation and a non-covalent intermediate, in addition to a covalent intermediate bound to the Cys residue at the active center during the catalytic cycle (Figure S7) (Griebel et al., 1968; Jia et al., 2000, 2001; Müh et al., 1999). Our asymmetric dimer supports the latter mechanism, as the distance between the two catalytic Cys residues is too far apart and only single CoA molecule binds the dimer. The movement of the His477 out of the catalytic pocket suggests His involved only in the initiation of the catalysis, which is also in agreement with the proposed *processive model*.

The fact that CoA lacking the 3′ phosphate and 3′-P-5′-P-ADP showed no inhibitory effect on PhaC activity (Ushimaru et al., 2013) suggests that both the 3′ phosphate and adenosine 3′,5′-bisphosphate moieties of CoA are required for CoA binding. It is likely that polar and electrostatic interactions such as salt bridge formation with the charged phosphate groups would stabilize CoA binding. However, such polar and electrostatic interactions were not observed in our current structure. It should be noted that the N-terminal end loop of PhaC$_{Cs}$-CAT is extended so as to interact with the CoA adenosine moiety, where Ile177 interacts with the adenine ring and ribose of the bound CoA molecule (Figure 5D). In this study, our construct of PhaC$_{Cs}$-CAT began at Phe175, and the first two residues were poorly defined, probably because of disordering. Interestingly, the N-flanking region contains polar residues containing Lys and Arg residues. For example, Lys174 is likely to interact with the phosphate group of CoA (Figure S3). The N-terminal flanking loop of PhaC$_{Cs}$-CAT is the linker between the N-terminal domain and the catalytic domain. We speculate that the linker may play an important role in CoA binding by interacting with the phosphate group.

One of the major questions that remains is the structure and function of the N-terminal domain of PhaC, which is absent in all the currently available structures of PhaCs. In our previous analytical size exclusion chromatography, full-length PhaC$_{Cs}$ exists in a monomer-dimer equilibrium, but PhaC$_{Cs}$-CAT exists only as a monomer (Chek et al., 2017). As the N-terminal domain assists in the dimerization of PhaC$_{Cs}$, it is reasonable to speculate that the N-terminal domain may regulate PHA biosynthesis through dimerization. This speculation remained to be confirmed until the structure of the N-terminal domain was determined.

In conclusion, we presented a structure of the CoA-bound form stabilized by the free form in the asymmetric dimer. The structure reveals the mechanism by which dynamic conformational changes enable PhaC to form the open conformation of the CoA-bound form. Our structure reveals valuable information concerning the conformational dynamics of the CAP subdomain and CoA binding. This may bring us a step closer to understand the catalytic mechanism involved and provide valuable clues in efforts directed at modifying this important enzyme with the aim of reducing petrochemical plastic waste pollution in the environment.

Limitations of the Study

Our structural study presented the first structure of the catalytic domain of PhaC, PhaC-CAT, in complex with a ligand, CoA, which is the by-product released from the substrate acyl-CoA. The structure reveals dynamic conformational changes in the catalytic domain to incorporate the substrate into the active site of one PhaC protomer but not the other protomer of the PhaC dimer. The asymmetric behavior of two protomers of the PhaC dimer is an unexpected finding, which enables us to understand part of the uncovered catalytic mechanism. At present, our knowledge of the three-dimensional structures of PhaC is limited to the catalytic domain, whereas the full-length molecule of PhaC possesses the N-terminal domain connected to the catalytic domain. Several data suggest that the N-terminal domain plays a role in stabilization of the PhaC dimerization and enhances the catalytic activity. It is the next step of our study to clarify the mechanism by which the N-terminal domain affects the PhaC dimerization and catalytic activity. It is unclear that the N-terminal domain may modify the dynamic properties of the conformation of the catalytic domain. To answer the question, we need to determine the three-dimensional structure of the full-length PhaC utilizing X-ray diffraction with the crystals and/or cryo-electron microscopy with single particle analysis. Nevertheless, our structure of PhaC-CAT provides valuable clues to modification of this important enzyme for industrial application to produce biodegrade plastics as an alternative to petroleum-derived plastics.

METHODS

All methods can be found in the accompanying Transparent Methods supplemental file.

DATA AND CODE AVAILABILITY

Coordinate and structure factor of $PhaC_{Cs}$-CAT + CoA complex has been deposited in the Protein Data-Bank under accession number 6K3C.

SUPPLEMENTAL INFORMATION

Supplemental Information can be found online at https://doi.org/10.1016/j.isci.2020.101084.

ACKNOWLEDGMENTS

This work was supported by the JST A-STEP Grant (29A1027 to T.H.) and the Research University Grant (RUI) from Universiti Sains Malaysia (USM) (1001/PBIOLOGI/8011060 to K.S.). The synchrotron radiation experiments were performed at BL41XU and BL44XU in SPring-8 with the approval of the Japan Synchrotron Radiation Research Institute (JASRI) (proposal nos. 2015A1086, 2015B2086, 2015A6549, 2015B6549, 2016A2510, 2016B2510, 2016A2519, 2016B2519, 2016A6648, 2016B6648, 2017A2502, 2017A6759, 2017B6759, 2018A2503, 2018A2529, 2018A2540, 2018A6855, 2018B2503, 2018B6855, 2019A2516, 2019A2576, 2019A6955, 2019B2516, 2019B6955, and 2019B2727). *Chromobacterium* sp. USM2 bacterium was provided by RIKEN BRC, which is participating in the National Bio-Resource Project of MEXT, Japan. We are grateful to Dr. Anthony J. Sinskey and Dr. Christopher Brigham for their generosity in providing the *C. necator* mutant host strains (Re2058) and plasmid pCB113 used in this study. M.F.C. also thanks Dr. Mohd Razip Samian (Universiti Sains Malaysia, retired) for his advice and discussion before the initiation of this project. M.F.C. was supported by the PhD scholarship (MEXT, Japan). H.T.T. was supported by the MyBrainSc scholarship (Ministry of Higher Education, Malaysia). H.T.T. also acknowledges the student travel funds provided by both USM (Post Graduate Research Attachment Fund) and NAIST.

AUTHOR CONTRIBUTIONS

T.H. and M.F.C. conceived the project and designed the experiments. K.S. provided the cDNA and expertise in PhaC enzymology. M.F.C., S.-Y.K., and T.M. executed the protein biochemistry, crystallization, and

data collection and solved and refined the structures, directed by T.H. M.F.C., S.-Y.K., and T.H. interpreted the data. M.F.C. executed the mutation studies and enzyme assays. H.T.T. executed the *in vivo* assay. M.F.C., S.-Y.K., and T.H. wrote the manuscript, and all authors reviewed the manuscript.

DECLARATION OF INTERESTS

The authors declare no competing financial interests.

Received: February 25, 2020
Revised: April 1, 2020
Accepted: April 15, 2020
Published: May 22, 2020

REFERENCES

Anderson, A.J., and Dawes, E.A. (1990). Occurrence, metabolism, metabolic role, and industrial uses of bacterial polyhydroxyalkanoates. Microbiol. Rev. *54*, 450–472.

Bhubalan, K., Kam, Y.C., Yong, K.H., and Sudesh, K. (2010a). Cloning and expression of the PHA synthase gene from a locally isolated *Chromobacterium* sp. Usm2. J. Basic Microbiol. *6*, 81–90.

Bhubalan, K., Rathi, D.-N.N., Abe, H., Iwata, T., and Sudesh, K. (2010b). Improved synthesis of P(3HB-co-3HV-co-3HHx) terpolymers by mutant *Cupriavidus necator* using the PHA synthase gene of *Chromobacterium* sp. USM2 with high affinity towards 3HV. Polym. Degrad. Stab. *95*, 1436–1442.

Bhubalan, K., Chuah, J.A., Shozui, F., Brigham, C.J., Taguchi, S., Sinskey, A.J., Rha, C., and Sudesh, K. (2011). Characterization of the highly active polyhydroxyalkanoate synthase of *Chromobacterium* sp. strain USM2. Appl. Environ. Microbiol. *77*, 2926–2933.

Chek, M.F., Kim, S.-Y., Mori, T., Arsad, H., Samian, M.R., Sudesh, K., and Hakoshima, T. (2017). Structure of polyhydroxyalkanoate (PHA) synthase PhaC from *Chromobacterium* sp. USM2, producing biodegradable plastics. Sci. Rep. *7*, 5312.

Chek, M.F., Hiroe, A., Hakoshima, T., Sudesh, K., and Taguchi, S. (2019). PHA synthase (PhaC): interpreting the functions of bioplastic-producing enzyme from a structural perspective. Appl. Microbiol. Biotechnol. *103*, 1131–1141.

Chen, G.Q., and Patel, M.K. (2012). Plastics derived from biological sources: present and future: a technical and environmental review. Chem. Rev. *112*, 2082–2099.

Chovancova, E., Pavelka, A., Benes, P., Strnad, O., Brezovsky, J., Kozlikova, B., Gora, A., Sustr, V., Klvana, M., Medek, P., et al. (2012). Caver 3.0: a tool for the analysis of transport pathways in dynamic protein structures. PLoS Comput. Biol. *8*, e1002708.

Doi, Y., Kanesawa, Y., Tanahashi, N., and Kumagai, Y. (1992). Biodegradation of microbial polyesters in the marine environment. Polym. Degrad. Stab. *36*, 173–177.

Doi, Y., Kitamura, S., and Abe, H. (1995). Microbial synthesis and characterization of poly (3-hydroxybutyrate-co-3-hydroxyhexanoate). Macromolecules *28*, 4822–4828.

Gao, D., Maehara, A., Yamane, T., and Ueda, S. (2001). Identification of the intracellular polyhydroxyalkanoate depolymerase gene of *Paracoccus denitrificans* and some properties of the gene product. FEMS Microbiol. Lett. *196*, 159–164.

Gerngross, T.U., and Martin, D.P. (1995). Enzyme-catalyzed synthesis of poly[(R)-(-)-3-hydroxybutyrate]: formation of macroscopic granules *in vitro*. Proc. Natl. Acad. Sci. U S A *92*, 6279–6283.

Gerngross, T.U., Snell, K.D., Peoples, O.P., Sinskey, a J., Csuhai, E., Masamune, S., and Stubbe, J. (1994). Overexpression and purification of the soluble polyhydroxyalkanoate synthase from *Alcaligenes eutrophus*: evidence for a required posttranslational modification for catalytic activity. Biochemistry *33*, 9311–9320.

Griebel, R., Smith, Z., and Merrick, J.M. (1968). Metabolism of poly-beta-hydroxybutyrate. I. Purification, composition, and properties of native poly-beta-hydroxybutyrate granules from *Bacillus megaterium*. Biochemistry *7*, 3676–3681.

Hiroe, A., Chek, M.F., Hakoshima, T., Sudesh, K., and Taguchi, S. (2019). Synthesis of Polyesters III: acyltransferase as catalyst. In Enzymatic Polymerization towards Green Polymer Chemistry, S. Kobayashi, H. Uyama, and J. Kadokawa, eds. (Springer Singapore), pp. 199–231.

Hopewell, J., Dvorak, R., and Kosior, E. (2009). Plastics recycling: challenges and opportunities. Philos. Trans. R. Soc. B Biol. Sci. *364*, 2115–2126.

Jambeck, J.R., Geyer, R., Wilcox, C., Siegler, T.R., Perryman, M., Andrady, A., Narayan, R., and Law, K.L. (2015). Plastic waste inputs from land into the ocean. Science *347*, 768–771.

Jia, Y., Kappock, T.J., Frick, T., Sinskey, A.J., and Stubbe, J. (2000). Lipases provide a new mechanistic model for polyhydroxybutyrate (PHB) synthases: characterization of the functional residues in *Chromatium vinosum* PHB synthase. Biochemistry *39*, 3927–3936.

Jia, Y., Yuan, W., Wodzinska, J., Park, C., Sinskey, A.J., and Stubbe, J. (2001). Mechanistic studies on class I polyhydroxybutyrate (PHB) synthase from *Ralstonia eutropha*: class I and III synthases share a similar catalytic mechanism. Biochemistry *40*, 1011–1019.

Kawaguchi, Y., and Doi, Y. (1992). Kinetics and mechanism of synthesis and degradation of poly(3-hydroxybutyrate) in *Alcaligenes eutrophus*. Macromolecules *25*, 2324–2329.

Kim, J., Kim, Y.-J., Choi, S.Y., Lee, S.Y., and Kim, K.-J. (2017). Crystal structure of *Ralstonia eutropha* polyhydroxyalkanoate synthase C-terminal domain and reaction mechanisms. Biotechnol. J. *12*, 1600648.

Lau, N.-S., Foong, C.P., Kurihara, Y., Sudesh, K., and Matsui, M. (2014). RNA-Seq analysis provides insights for understanding photoautotrophic polyhydroxyalkanoate production in recombinant *Synechocystis* Sp. PLoS One *9*, e86368.

Mergaert, J., Webb, A., Anderson, C., Wouters, A., and Swings, J. (1993). Microbial degradation of poly(3-hydroxybutyrate) and poly(3-hydroxybutyrate-co-3-hydroxyvalerate) in soils. Appl. Environ. Microbiol. *59*, 3233–3238.

Meng, D.-C., Shen, R., Yao, H., Chen, J.-C., Wu, Q., and Chen, G.-Q. (2014). Engineering the diversity of polyesters. Curr. Opin. Biotechnol. *29*, 24–33.

Müh, U., Sinskey, A.J., Kirby, D.P., Lane, W.S., and Stubbe, J. (1999). PHA synthase from *Chromatium vinosum*: cysteine 149 is involved in covalent catalysis. Biochemistry *38*, 826–837.

North, E.J., and Halden, R.U. (2013). Plastics and environmental health: the road ahead. Rev. Environ. Health *28*, 1–8.

Park, S.J., Choi, J. Il, and Lee, S.Y. (2005). Short-chain-length polyhydroxyalkanoates: synthesis in metabolically engineered *Escherichia coli* and medical applications. J. Microbiol. Biotechnol. *15*, 206–215.

Peoples, O.P., and Sinskey, A.J. (1989). Poly-beta-hydroxybutyrate (PHB) biosynthesis in *Alcaligenes eutrophus* H16. Identification and characterization of the PHB polymerase gene (phbC). J. Biol. Chem. *264*, 15298–15303.

Pötter, M., and Steinbüchel, A. (2005). Poly(3-hydroxybutyrate) granule-associated proteins: impacts on poly(3-hydroxybutyrate) synthesis and degradation. Biomacromolecules *6*, 552–560.

Rehm, B.H.A. (2003). Polyester synthases: natural catalysts for plastics. Biochem. J. *376*, 15–33.

Rehm, B.H.A., Antonio, R.V., Spiekermann, P., Amara, A.A., and Steinbüchel, A. (2002). Molecular characterization of the poly(3-hydroxybutyrate) (PHB) synthase from *Ralstonia eutropha: in vitro* evolution, site-specific mutagenesis and development of a PHB synthase protein model. Biochim. Biophys. Acta *1594*, 178–190.

Sagong, H.-Y., Son, H.F., Choi, S.Y., Lee, S.Y., and Kim, K.-J. (2018). Structural insights into polyhydroxyalkanoates biosynthesis. Trends Biochem. Sci. *43*, 790–805.

Schubert, P., Steinbüchel, A., and Schlegel, H.G. (1988). Cloning of the *Alcaligenes eutrophus* genes for synthesis of poly-beta-hydroxybutyric acid (PHB) and synthesis of PHB in *Escherichia coli*. J. Bacteriol. *170*, 5837–5847.

Snell, K.D., Singh, V., and Brumbley, S.M. (2015). Production of novel biopolymers in plants: recent technological advances and future prospects. Curr. Opin. Biotechnol. *32*, 68–75.

Stubbe, J., and Tian, J. (2003). Polyhydroxyalkanoate (PHA) hemeostasis: the role of PHA synthase. Nat. Prod. Rep. *20*, 445–457.

Stubbe, J., Tian, J., He, A., Sinskey, A.J., Lawrence, A.G., and Liu, P. (2005). Nontemplate-dependent polymerization processes: polyhydroxyalkanoate synthases as a paradigm. Annu. Rev. Biochem. *74*, 433–480.

Sudesh, K., Abe, H., and Doi, Y. (2000). Synthesis, structure and properties of polyhydroxyalkanoates: biological polyesters. Prog. Polym. Sci. *25*, 1503–1555.

Taguchi, S., and Doi, Y. (2004). Evolution of polyhydroxyalkanoate (PHA) production system by "enzyme evolution": successful case studies of directed evolution. Macromol. Biosci. *4*, 145–156.

Tian, J., Sinskey, A.J., and Stubbe, J. (2005). Detection of intermediates from the polymerization reaction catalyzed by a D302A mutant of class III polyhydroxyalkanoate (PHA) synthase. Biochemistry *44*, 1495–1503.

Ushimaru, K., Sangiambut, S., Thomson, N., Sivaniah, E., and Tsuge, T. (2013). New insights into activation and substrate recognition of polyhydroxyalkanoate synthase from *Ralstonia eutropha*. Appl. Microbiol. Biotechnol. *97*, 1175–1182.

Wang, Q., Zhuang, Q., Liang, Q., and Qi, Q. (2013). Polyhydroxyalkanoic acids from structurally-unrelated carbon sources in *Escherichia coli*. Appl. Microbiol. Biotechnol. *97*, 3301–3307.

Williams, S.F., and Martin, D.P. (2005). Applications of polyhydroxyalkanoates (PHA) in medicine and pharmacy. In Biopolymers Online, A. Steinbüchel, ed. (Wiley-VCH Verlag GmbH & Co. KGaA). https://doi.org/10.1002/3527600035.bpol4004.

Wittenborn, E.C., Jost, M., Wei, Y., Stubbe, J., and Drennan, C.L. (2016). Structure of the catalytic domain of the class I polyhydroxybutyrate synthase from *Cupriavidus necator*. J. Biol. Chem. *291*, 25264–25277.

Wodzinska, J., Snell, K.D., Rhomberg, A., Sinskey, A.J., Biemann, K., and Stubbe, J. (1996). Polyhydroxybutyrate synthase: evidence for covalent catalysis. J. Am. Chem. Soc. *118*, 6319–6320.

Zhang, W., Chen, C., Cao, R., Maurmann, L., and Li, P. (2015). Inhibitors of polyhydroxyalkanoate (PHA) synthases: synthesis, molecular docking, and implications. ChemBioChem *16*, 156–166.

Zinn, M., Witholt, B., and Egli, T. (2001). Occurrence, synthesis and medical application of bacterial polyhydroxyalkanoate. Adv. Drug Deliv. Rev. *53*, 5–21.

iScience, Volume *23*

Supplemental Information

Asymmetric Open-Closed Dimer Mechanism of Polyhydroxyalkanoate Synthase PhaC

Min Fey Chek, Sun-Yong Kim, Tomoyuki Mori, Hua Tiang Tan, Kumar Sudesh, and Toshio Hakoshima

TRANSPARENT METHODS

KEY RESOURCES TABLE

REAGENT or RESOURCE	SOURCE	IDENTIFIER
Chemicals, Peptides, and Recombinant Proteins		
LB Broth, Lennox	Nacalai	Cat# 20066-24
isopropyl-β-D-thiogalactoside	FUJIFILM Wako	Cat# 093-05011
β-mercaptoethanol	FUJIFILM Wako	Cat# 131-14572
Tris	FUJIFILM Wako	Cat# 512-97505
Sodium acetate	FUJIFILM Wako	Cat# 192-01075
Coenzyme A	Sigma-Aldrich	Cat# C3019
Poly(ethylene glycol) BioUltra, 3,350	Sigma-Aldrich	Cat# 88276
5,5'-Dithiobis(2-nitrobenzoic acid) (DTNB)	Sigma-Aldrich	Cat# D8130
DL-β-Hydroxybutyryl coenzyme A	Sigma-Aldrich	Cat# H0261
PreScission Protease	GE Healthcare	Cat# 27084301
Bacterial and Virus Strains		
Chromobacterium sp. USM2	RIKEN BRC	JCM15051
E. coli Rosetta™ 2 (DE3)	Novagen	71397
C. necator strains Re2058	Budde *et al.*, 2011	H16 Δ*phaC1*, Δ*proC*
E. coli strains DH5α	Toyobo	General cloning strain
E. coli strains S17-1	Simon *et al.*, 1983	Strain for transfer plasmid to *C. necator* Re2058
Deposited Data		
Crystal structure of $PhaC_{Cs}$-CAT + CoA	This study	PDB: 6K3C
Recombinant DNA		
pET47b (+)	Novagen	71461
PhaCcs in pET47b (+)	This study	N/A
PhaCcs-CAT 175-567 (D447N) in pET47b (+)	This study	N/A
Full-length PhaCcs 1-567 (S363A) in pET47b (+)	This study	N/A
Full-length PhaCcs 1-567 (R365A) in pET47b (+)	This study	N/A
Full-length PhaCcs 1-567 (D368A) in pET47b (+)	This study	N/A
Full-length PhaCcs 1-567 (R409A) in pET47b (+)	This study	N/A
pCB113 (pBBR1MCS-2 with $PhaC2_{Ra}$-*phaA*-$phaJ1_{Pa}$ and *proC*)	Budde *et al.*, 2011	
pHT1 (Derived from pCB113 by removing *phaC2* of *Rhodococcus aetherivorans* I24 inside the plasmid)	This study	
pHT1-$phaC_{Cs}$	This study	Wild-type
pHT1-$phaC_{Cs}$ S363A	This study	S363A
pHT1-$phaC_{Cs}$ R365A	This study	R365A
pHT1-$phaC_{Cs}$ D368A	This study	D368A
pHT1-$phaC_{Cs}$ R409A	This study	R409A
Oligonucleotides (primers 5' – 3')		
PhaCcs_D447N_F	ATG TTC GCC GCG CGC GAA AAC CAC ATC GTG CTG TGG AGT	
PhaCcs_D447N_R	ACT CCA CAG CAC GAT GTG GTT TTC GCG CGC GGC GAA CAT	
PhaCcs_S363A_F	GGA CGC ACT TTC GCC GCC CTG CGC GCC AAC GAC CTG	
PhaCcs_S363A_F	CAG GTC GTT GGC GCG CAG GGC GGC GAA AGT GCG TCC	
PhaCcs_R365A_F	ACT TTC GCC AGC CTG GCC GCC AAC GAC CTG GTG TGG	
PhaCcs_R365A_R	CCA CAC CAG GTC GTT GGC GGC CAG GCT GGC GAA AGT	

PhaCcs_D368A_F	AGC CTG CGC GCC AAC GCC CTG GTG TGG AAC TAC GTC	
PhaCcs_D368A_R	GAC GTA GTT CCA CAC CAG GGC GTT GGC GCG CAG GCT	
PhaCcs_R409A_F	CAC ACC TTC ATG CTG GCG CAG TTC TAC ATC AAC AAC	
PhaCcs_R409A_R	GTT GTT GAT GTA GAA CTG CGC CAG CAT GAA GGT GTG	
phaC$_{Cs}$_SwaI_F	ATC**ATTTAAAT**AGGAGGAGGCGCATGCAGCAGTTTGTCAATTCCCTG	
phaC$_{Cs}$_SwaI_R	AGC**ATTTAAAT**TCAGTTCAAGGCGGCGGCGAC	
Software and Algorithm		
HKL2000	Otwinowski and Minor, 1997	N/A
PHENIX	Adams et al., 2010	N/A
PHASER	McCoy et al., 2007	N/A
CCP4i	Winn et al., 2011	N/A
COOT	Emsley and Cowtan, 2004	N/A
LSQKAB in CCP4 suite	Kabsch, 1976	N/A
Areaimol in CCP4 suite	Lee and Richards, 1971; Saff and Kuijlaars, 1997	N/A
PyMOL	DeLano Scientific	N/A
CAVER	Chovancova et al., 2012	N/A
Other		
Hiload Superdex 200 26/600	GE Healthcare	28989336
Hitrap-Q HP	GE Healthcare	17115401
Ni-NTA agarose	QIAGEN	30210
AMICON ULTRA-15 15ML - 30 KDa cutoff	Merck Millipore	UFC903024
UV-Visible Spectrophotometer (w/ Thermoelectrically Temperature Controlled Cell Holder)	Shimadzu	UV1800 TCC-100
SBP-1 Capillary GC column	Sigma	-
Gas chromatograph equipped with AOC-20i Auto injector	Shimadzu	-

Cloning, expression and purification.

DNA encoding the catalytic domain of PhaC$_{Cs}$, *phaC*$_{Cs}$*-CAT* (1179 nucleotides) was cloned from *Chromobacterium* sp. USM2 (JCM15051, RIKEN BRC) and inserted into His-fusion vector pET47b [+] (Novagen). The catalytic mutant Asp447Asn of PhaC$_{Cs}$-CAT was generated by PCR site-directed mutagenesis using wild-type plasmid as template, and the integrity of the coding region was verified by DNA sequencing. The primers used in the construction of the mutants were shown in Key Resources Table. The catalytic mutant plasmid was transformed into *Escherichia coli* Rosetta 2 (DE3) (Novagen) and cells were grown in LB medium supplemented with 50 µg/ml Kanamycin and 35 µg/ml Chloramphenicol at 37˚C until the OD_{600nm} reached a value of 0.6. Protein expression was induced by the addition of isopropyl-β-D-thiogalactoside (IPTG) to a final concentration of 100 µM. The culture was induced for another 20 hours at 20˚C and cells were harvested by centrifugation. Cells were then suspended in 2X PBS (phosphate-buffered saline) with 3 mM β-mercaptoethanol (β-ME) and disrupted by sonication in an ice bath. The soluble fraction

was separated by ultracentrifugation and then loaded onto a Ni-NTA agarose column (QIAGEN). The column was washed with buffer containing 20 mM Tris-HCl (pH 8.0), 100 mM NaCl, 3 mM β-ME and 10 mM Imidazole, and target protein was eluted using the same buffer containing 250 mM Imidazole *in lieu* of 10 mM Imidazole. The column effluent was loaded onto a HiTrap Q anion-exchange column (GE Healthcare) and eluted using a gradient of 0-500 mM NaCl in buffer containing 20 mM Tris-HCl (pH 8.5) and 3 mM β-ME. The eluted products were pooled and digested overnight at 4˚C using PreScission protease (GE Healthcare). The digested product was loaded onto a Ni-NTA agarose column to remove the His-tag and co-purified products. Flow-through from the column was collected and concentrated by centrifugation using an Amicon Ultra 30,000 molecular weight cut-off filter (Merck Millipore). The concentrated product was finally passed through a Superdex 200 gel filtration column (GE Healthcare) using buffer comprising 10 mM Tris-HCl (pH 8.0), 100 mM NaCl and 3 mM β-ME. Peak fractions were collected and concentrated to about 50 mg/ml. SDS-PAGE of the protein samples gave one major band corresponding to ~43 kDa (PhaC$_{Cs}$-CAT). Analysis of the sample using matrix-assisted laser desorption/ ionization time-of-flight mass spectrometry (MALDI-TOF MS; Bruker Daltonics) confirmed that the target proteins were successfully purified without degradation. Two additional vector-derived residues (Gly-Pro) were identified at the N-terminus. Samples were frozen in liquid nitrogen and stored at -80˚C until use.

Crystallization.

Preliminary co-crystallization screening was performed by a vapor-diffusion method at both 4˚C and 20˚C using commercially available screening kits (Hampton Research and QIAGEN). To prepare the stable PhaC$_{Cs}$-CAT+CoA complex, PhaC$_{Cs}$-CAT (D447N) (0.3 mM) was mixed with CoA (12 mM) in equilibration buffer containing 10 mM Tris-Cl (pH 8.0), 100 mM NaCl and 3 mM β-ME. The mixture was incubated at 30°C for 30 minutes prior to crystallization set-up. The first hit was a cluster of crystals observed in equilibrium against mother liquor containing 0.2 M sodium acetate and 20% PEG3350 (QIAGEN) at 4˚C. The optimized crystals were grown in 5 days using a streak-seeding method against a self-made mother liquor containing 0.1 M Tris-Cl (pH 7.0), 0.015 M sodium acetate and 9% PEG3350 at 4˚C. Crystals were cryoprotected in the same mother liquor with 38-40% PEG3350.

X-ray data collection, phasing, refinement, and structural analyses.

All X-ray data were collected at SPring-8, Harima, Japan. During X-ray beam exposure, crystals were flash-cooled and maintained at 100 K using a nitrogen stream. Detailed statistics of the structure determination are shown in Table S1. All diffraction data were indexed and merged using the DENZO and SCALEPACK programs included in HKL2000 (Otwinowski and Minor, 1997). Phases of the PhaC$_{Cs}$-CAT+CoA complex structure were solved by molecular replacement using the Phaser program (McCoy et al., 2007) with the free form structure of PhaC$_{Cs}$-CAT (PDB code 5XAV) as a search model. The model structure was further refined using phenix.refine (Adams et al., 2010) and manually adjusted using Coot (Emsley and Cowtan, 2004). Coordinate and structure factor of PhaC$_{Cs}$-CAT+CoA complex has been deposited in the Protein Data Bank under accession number 6K3C. Superposition of the PhaCs was performed using the program LSQKAB (Kabsch, 1976) Illustrations and video (rigimol method) were prepared using the program PyMOL (DeLano Scientific). The dynamic transition video was edited and processed using Adobe Premiere Elements 15 (Adobe). The buried accessible surface area (ASA) of the dimer was calculated using program Areaimol (Lee and Richards, 1971; Saff and Kuijlaars, 1997) in CCP4 suite (Winn et al., 2011). The analysis and visualization of tunnels and channels in PhaC$_{Cs}$-CAT was calculated using the program CAVER (Chovancova et al., 2012).

Substrate Docking.

Substrates 3HB-CoA and 3HHx-CoA were modelled and docked into the catalytic pocket of the open form PhaC$_{Cs}$-CAT by Coot (Emsley and Cowtan, 2004), and followed by geometry minimization performed using Phenix.

***In vitro* enzymatic assay.**

The full-length wild type and mutated PHA synthase gene (*phaC*$_{Cs}$) from *Chromobacterium* sp. USM2 was constructed through In-Fusion cloning method (Takara Bio) in pET-47. The resulting plasmids were transformed into *Escherichia coli* DH5α then further transform to *E. coli* Rosetta 2 (DE3) (Novagen). The successful transformants were further verified by running colony polymerase chain reaction (PCR) and DNA sequencing. PHA synthase activity assays were performed by measuring the CoA released from the substrates during the polymerization process (Bhubalan et al., 2011). The 30˚C pre-incubated reaction mixture contained 100 mM Tris-Cl

(pH7.8), 0.15 mM (*R*)-3HBCoA and 0.15 mM DTNB. Reactions were commenced by mixing appropriate amounts of wild-type and catalytic mutant full-length PhaC_{Cs}. The release of CoA was measured at OD_{412nm} using a UV1800 instrument (Shimadzu) with temperature fixed at 30˚C. Expression and purification of full-length wild-type and mutant PhaC_{Cs} were performed using the same protocol as described earlier. All reactions were performed in triplicate.

Construction of bacterial strains. PCR was performed to amplify the wild type and mutated *pha*C_{Cs} from pET-47 previously constructed by using high-fidelity DNA polymerase (Lucigen Corporation, USA). The PCR products were digested with *Swa*I FastDigest restriction enzymes (ThermoScientific, USA) and then ligated to digested pHT1 plasmid using DNA Ligation Kit Ver. 2.1 (Takara Bio Inc., Japan) according to the manufacturer's protocol. The resulting plasmids were transformed into *E. coli* S17-1, and further transconjugate into *Cupriavidus necator* Re2058. The integrity of the transformed plasmids were verified by DNA sequencing. The strains and plasmids used in the study and the sequences of all oligonucleotide primers used in the construction of plasmids were listed in the key resource table. The ribosome binding sequences (RBS) were underlined. Bolded letters represent the digestion sites of the restriction enzymes.

***In vivo* PHA synthesis.**

PHA-negative strain, *C. necator* Re2058 was used as the host strain for PHA production. The recombinant plasmid pHT1-*pha*C_{Cs} that harbouring the *Chromobacterium* sp. USM2 synthase was used for expression of PHA synthase in *C. necator* Re2058. PHA accumulation were carried out via one-stage cultivation. *C. necator* transformants were first pre-cultured in nutrient rich (NR) medium (Doi et al.,1995) and transferred (3 % [v/v]) into 50 mL mineral medium (MM) (Budde et al., 2010) in 250 mL Erlenmeyer flask when its optical density (OD) reached approximately 4.0 – 5.0. Urea was supplemented as nitrogen source at final concentrations of 0.054 % while crude palm kernel oil (CPKO) was added as the sole carbon source at a final concentration of 0.6 % (v/v). Kanamycin (50 mg/L) was added to maintain plasmid in the cells. Cultures were grown at 30 °C, 200rpm for 48 h. After 48 h of cultivation, the cells were harvested, and lyophilized.

Analysis of PHA produced by the transformants.

The PHA content and composition in the cells was determined by using gas chromatography (GC).

The lyophilized cells (approximately 15-20 mg) were then subjected to methanolysis by using 15 % (v/v) sulfuric acid and 85 % (v/v) methanol at 100 °C for 140 min (Braunegg *et al.*, 1978). Caprylic acid methyl ester (CME) solution was used as an internal standard to determine the PHA content and its composition. The resulting methyl esters were analysed using gas chromatograph (Shimadzu, Japan) equipped with AOC-20i Auto injector (Shimadzu, Japan), SBP-1 Capillary GC column (Sigma, USA) and a flame ionization detector with nitrogen gas as carrier. The injector's temperature was set at 270 °C, the column's temperature was 70 °C and gradually increase to 280 °C with the rate of 10 °C/min, whereas the detector's temperature was set at 280 °C.

Supplemental References

Adams, P.D., Afonine, P. V., Bunkóczi, G., Chen, V.B., Davis, I.W., Echols, N., Headd, J.J., Hung, L.W., Kapral, G.J., Grosse-Kunstleve, R.W., et al. (2010). PHENIX: A comprehensive Python-based system for macromolecular structure solution. Acta Crystallogr. Sect. D Biol. Crystallogr. *66*, 213–221.

Bhubalan, K., Chuah, J.A., Shozui, F., Brigham, C.J., Taguchi, S., Sinskey, A.J., Rha, C., and Sudesh, K. (2011). Characterization of the highly active polyhydroxyalkanoate synthase of *Chromobacterium* sp. strain USM2. Appl. Environ. Microbiol. *77*, 2926–2933.

Braunegg, G., Sonnleitner, B., and Lafferty, R.M. (1978). A rapid gas chromatographic method for the determination of poly-β-hydroxybutyric acid in microbial biomass. Eur. J. Appl. Microbiol. Biotechnol. 6, 29–37.

Budde, C.F., Mahan, A.E., Lu, J., Rha, C., and Sinskey, A.J. (2010). Roles of multiple acetoacetyl coenzyme A reductases in polyhydroxybutyrate biosynthesis in *Ralstonia eutropha* H16. J. Bacteriol. *192*, 5319–5328.

Budde, C.F., Riedel, S.L., Willis, L.B., Rha, C., and Sinskey, A.J. (2011). Production of poly(3-hydroxybutyrate-co-3-hydroxyhexanoate) from plant oil by engineered *Ralstonia eutropha* strains. Appl. Environ. Microbiol. *77*, 2847–2854.

Chovancova, E., Pavelka, A., Benes, P., Strnad, O., Brezovsky, J., Kozlikova, B., Gora, A., Sustr, V., Klvana, M., Medek, P., et al. (2012). CAVER 3.0: a tool for the analysis of transport pathways in dynamic protein structures. PLoS Comput. Biol. *8*, e1002708.

Doi, Y., Kitamura, S., and Abe, H. (1995). Microbial synthesis and characterization of poly (3-hydroxybutyrate-co-3-hydroxyhexanoate). Macromolecules *28*, 4822–4828.

Emsley, P., and Cowtan, K. (2004). Coot: Model-building tools for molecular graphics. Acta Crystallogr. Sect. D Biol. Crystallogr. *60*, 2126–2132.

Kabsch, W. (1976). A solution for the best rotation to relate two sets of vectors. Acta Crystallogr. Sect. A

32, 922–923.

Lee, B., and Richards, F.M. (1971). The interpretation of protein structures: estimation of static accessibility. J. Mol. Biol. *55*, 379–400.

McCoy, A.J., Grosse-Kunstleve, R.W., Adams, P.D., Winn, M.D., Storoni, L.C., and Read, R.J. (2007). Phaser crystallographic software. J. Appl. Crystallogr. *40*, 658–674.

Otwinowski, Z., and Minor, W. (1997). Processing of X-ray diffraction data collected in oscillation mode. Methods Enzymol. *276*, 307–326.

Saff, E.B., and Kuijlaars, A.B.J. (1997). Distributing many points on a sphere. Math. Intell. *19*, 5–11.

Simon, R., Priefer, U., and Pühler, A. (1983). A broad host range mobilization system for *in vivo* genetic engineering: transposon mutagenesis in gram negative bacteria. Nature Biotechnology *1*, 784–791.

Winn, M.D., Ballard, C.C., Cowtan, K.D., Dodson, E.J., Emsley, P., Evans, P.R., Keegan, R.M., Krissinel, E.B., Leslie, A.G.W., McCoy, A., et al. (2011). Overview of the CCP4 suite and current developments. Acta Crystallogr. D. Biol. Crystallogr. *67*, 235–242.

SUPPLEMENTAL FIGURES AND TABLE

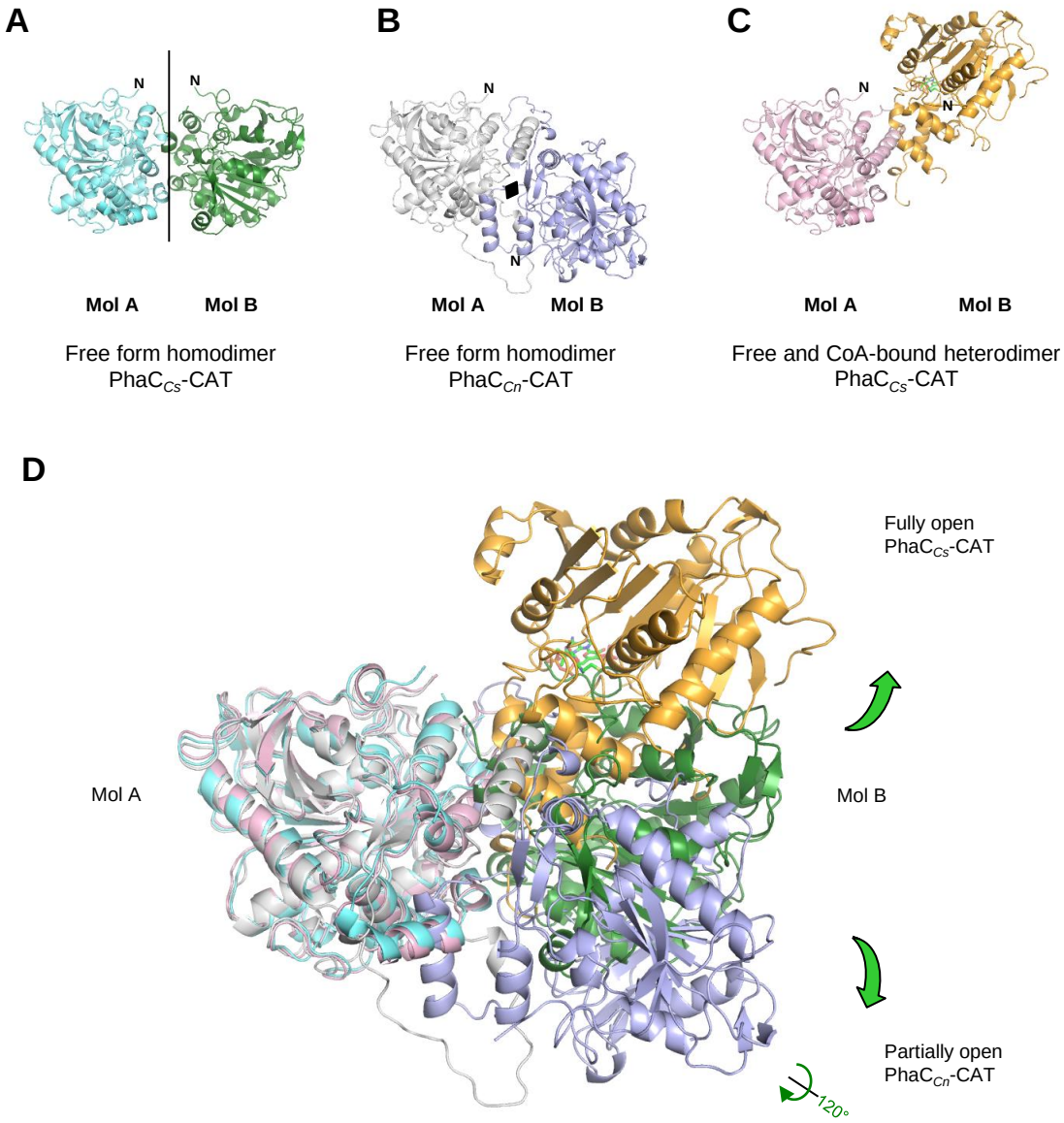

Figure S1. Conformational changes in the CAP subdomains induce changes in dimeric organization, Related to Figure 2.

(A) The homodimer of the free form of PhaC$_{Cs}$-CAT (PDB 5XAV). The protomers are related by pseudo-dyad symmetry (the dyad axis is shown with a line) and both display a closed conformation with the partly disordered LID region. The N-terminal end distance is 35.2 Å.
(B) The homodimer of the free form of PhaC$_{Cn}$-CAT (PDB 5HZ2) as viewed with Mol A in the same orientation with Mol A in the PhaC$_{Cs}$-CAT homodimer in (A). The protomers are related by dyad symmetry (the dyad axis is shown with a diamond) and both display a partially open conformation.
(C) The heterodimer between the free and CoA-bound forms of PhaC$_{Cs}$-CAT (this study). The free form (Mol A) is viewed in the same orientation with Mol A in the PhaC$_{Cs}$-CAT homodimer in (A). The N-terminal end distance is 39.2 Å.
(D) Structural overlay of the heterodimer between the closed free form and the open CoA-bound form of PhaC$_{Cs}$-CAT (this study) on the closed PhaC$_{Cs}$-CAT homodimer (PDB 5XAV), and the partially open PhaC$_{Cn}$-CAT homodimer (PDB 5ZH2). Color codes are the same as in Figures S1A-C.

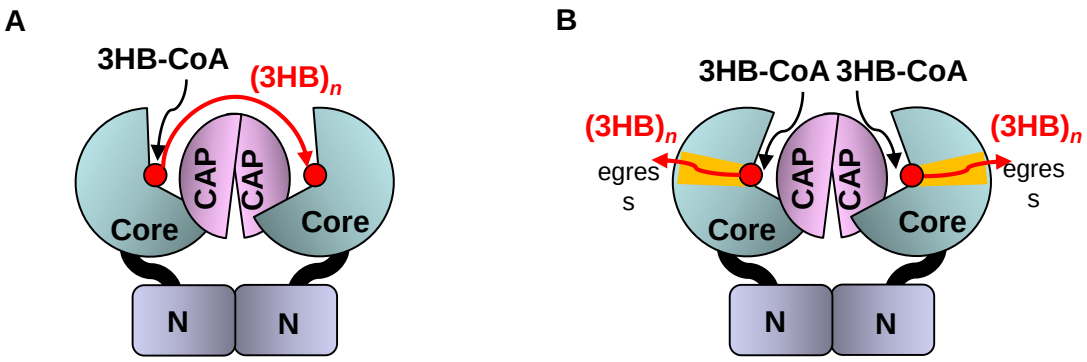

Figure S2. A model of proposed catalysis mechanism of PhaC, Related to Figure 1.

(A) A non-processive model of the proposed catalytic mechanism, where 2 catalytic Cys residues are required for the ping-pong transfer mechanism during the elongation process. The N domain is proposed to contribute to stabilization of the dimer.
(B) A processive model of the proposed catalytic mechanism. The polymerization happen with a single catalytic Cys residue and the elongating polymer grows to the surface through a product egress pathway (orange-colored). The N domain is proposed to contribute to stabilization of the dimer.

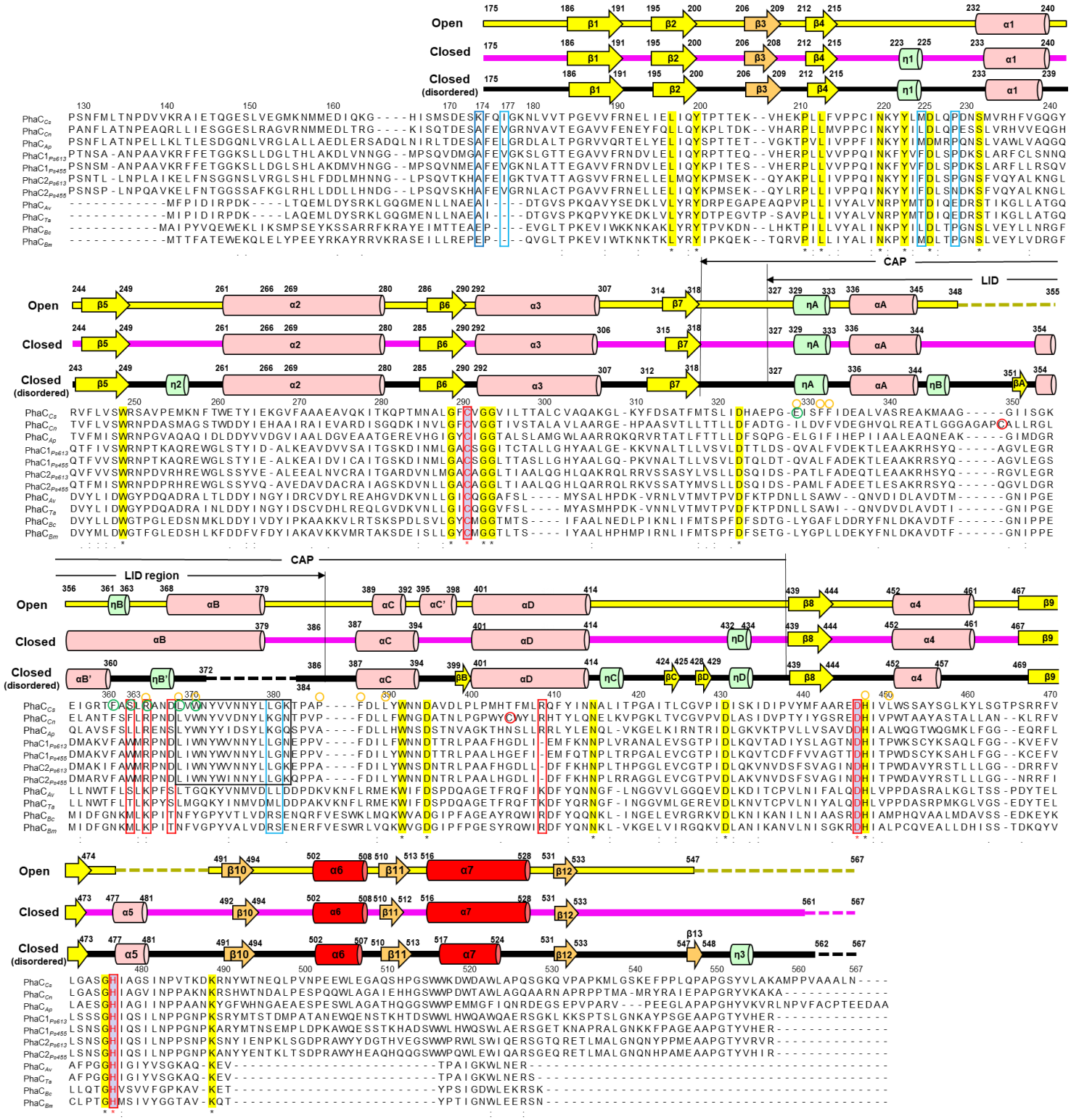

Figure S3. Alignment of amino acid sequences of PhaC catalytic domains, Related to Figure 4, 5, 6, 7I.

The secondary structure elements found in the structures of the open conformation of the CoA-bound form (Open, yellow-colored bar) and the closed conformation of the free form (Closed, magenta-colored bar) forming the PhaC$_{Cs}$-CAT heterodimer (this study), and the closed conformation of the free form (Closed (disordered), black-colored bar) of PhaC$_{Cs}$-CAT forming a homodimer (PDB 5XAV) are shown at the top of the alignment with α-helices (pink cylinders), β-strands (yellow arrows), loops (bold lines) and missing loops (broken lines). Catalytic residues forming the triad Cys-His-Asp are shown in red and are boxed. Conserved residues are highlighted in yellow. Glu329, Phe332, Phe333, Arg365, His448 and Val450 of PhaC$_{Cs}$-CAT are marked with orange circles at the top. Two Cys residues (Cys382 and Cys438 of PhaC$_{Cn}$-CAT) forming a disulfide bond are marked by red circles. The residues involved in the dimerization are marked by green circles, which includes W371, F361, L369, N367, R365, E329, and S363 (**Related to Figure 4**). The residues involved in the CoA-binding were boxed in light blue frames, which includes I177, M225, P229, main chain of L380 and G381. While K174 (dark blue frame) is expected to interact with the phosphate group of CoA (**Related to Figure 5**). Part (Leu402–Asn415 of PhaC$_{Cn}$-CAT) of the LID region forming α4 helix in the structure is conserved in members of Class I and II synthases. These sequences are marked by a black box (**Related to Figure 6**). The candidates for mutational studies on S363A, R365A, D368A, R409A are boxed in red frames (**Related to Figure 7I**).

*The abbreviations are as follows: Class I: PhaC$_{Cs}$ (*Chromobacterium* sp. USM2 (ADL70203)), PhaC$_{Cn}$ (*Cupriavidus necator* (AAW65074)), PhaC$_{Ap}$ (*Aeromonas punctata* (BAA21815)); Class II: PhaC1, C2$_{Ps61\text{-}3}$ (*Pseudomonas* sp. 61-3 (BAA36200, BAA36202), PhaC1,C2$_{PsUSM4\text{-}55}$ *Pseudomonas* sp. USM4-55 (ABX64434, ABX64435); Class III: PhaC$_{Av}$ (*Allochromatium vinosum* DSM180 (BAE20055)), PhaC$_{Tv}$ (*Thiocystis violascens* DSM198 (AFL75311)); Class IV: PhaC$_{Bc}$ (*Bacillus cereus* (BAI68395)), PhaC$_{Bm}$ (*Bacillus megaterium* (AAD05260))

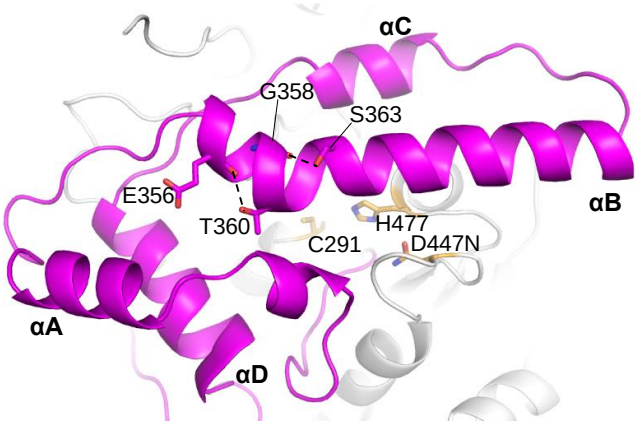

Figure S4. Kinking of long αB helix of the free form, Related to Figure 3B.

Long αB helix of the free form of the PhaC$_{Cs}$-CAT heterodimer is kinked at Thr360. The kink is induced by side chain-side chain interaction. The regular main chain-main chain hydrogen bonds of the helix are disturbed by the side chains of Thr360 and Ser363 residues, which form hydrogen bonds with main-chain amide groups of the helix.

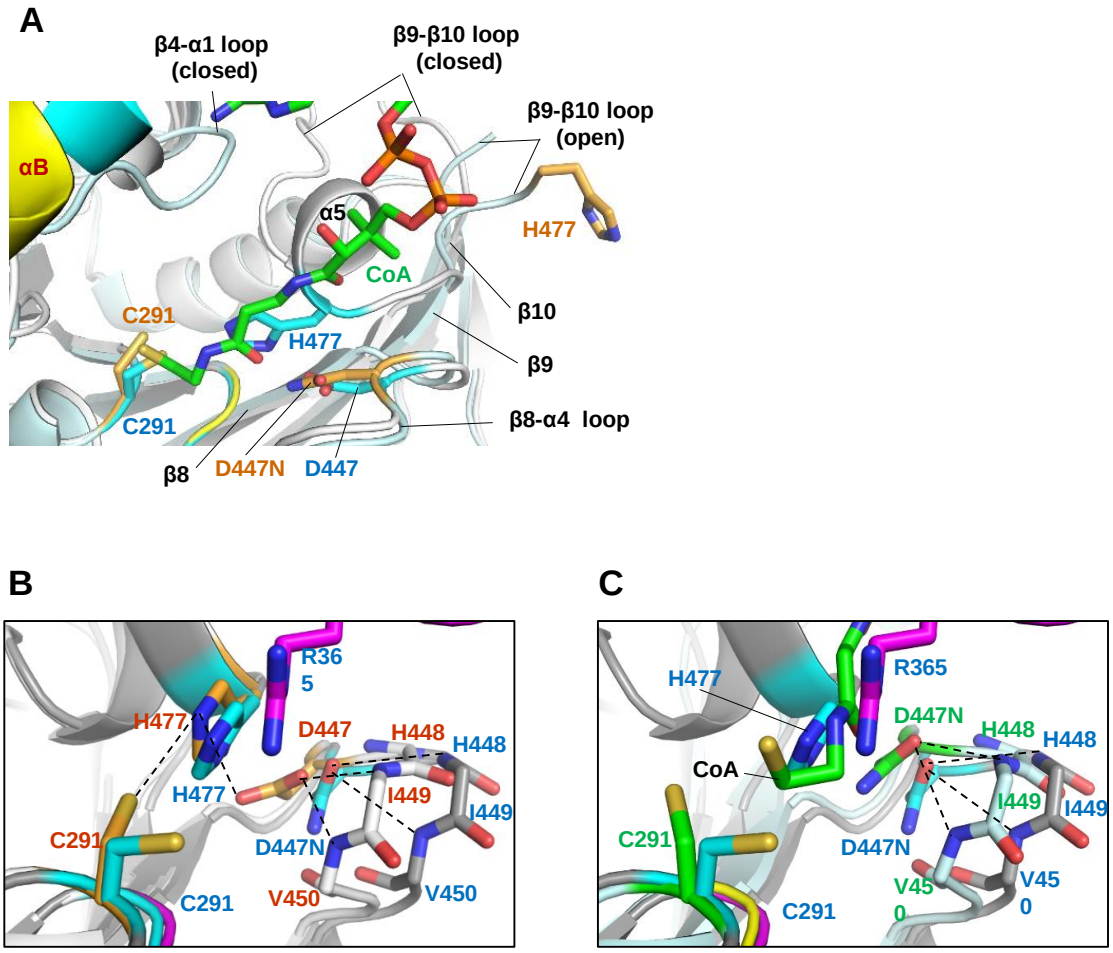

Figure S5. Comparison of the catalytic triads, Related to Figure 5.

(A) Overlay of catalytic triads from the CoA-bound (yellow) and free (cyan) forms of $PhaC_{Cs}$-CAT. While C291 and D447/D447N are well overlapped, His477 is shifted out from the catalytic site. CoA is shown in green stick model in this figure.
(B) Overlay of the catalytic triad of the free form (Mol A, cyan) in the closed conformation of the current $PhaC_{Cs}$-CAT heterodimer onto that of the free form (orange) in the partly closed conformation of the $PhaC_{Cs}$-CAT homodimer (PDB 5XAV; Chek *et al*., 2017). In the closed conformation, Arg365 (magenta) modified the geometry of the triad.
(C) Overlay of the catalytic triads of the free form (Mol A, cyan) of $PhaC_{Cs}$-CAT in the open conformation onto the CoA-bound form (Mol B, green) in the open conformation. Asn367(B) of the CoA-bound form does not participate in intermolecular interactions but plays a role as the N-terminal cap of αB helix by forming intramolecular hydrogen bonds with the N-terminal end of αB helix and the flanking loop (the main chains of Leu364(B), Arg365(B), Asp368(B) and Leu369(B)).

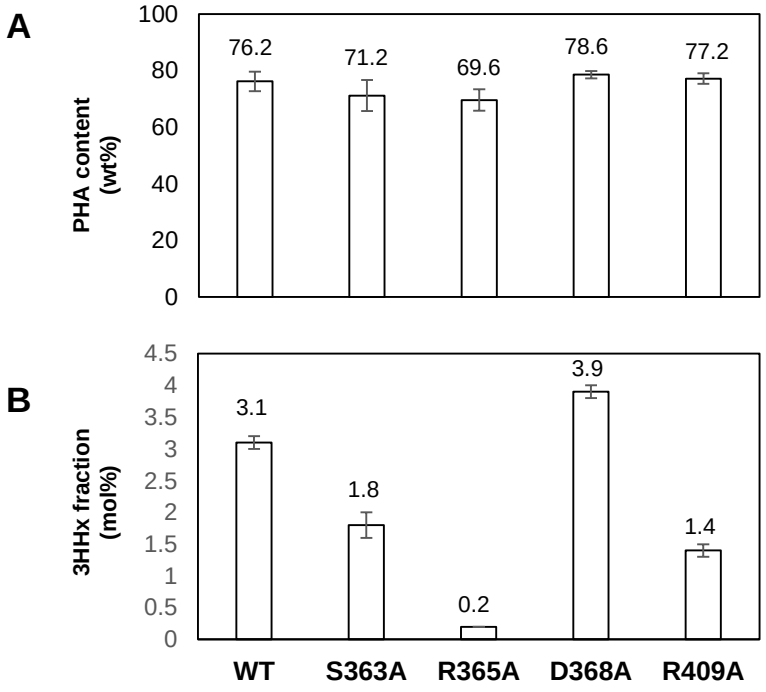

Figure S6. Polyhydroxyalkanoate production by transformants *Cupriavidus necator* Re2058 harboring mutated phaC$_{Cs}$ genes from CPKO[a], Related to Figure 7I.

(A) All mutants, S363A, R365A, D368A, R409A are capable of accumulate similar PHA content as in the wild-type.
(B) All mutants showed lower 3HHx fractions in the PHA content except D368A. The D368A mutant incorporated 3.9 mol% of 3HHx, which is higher than that of the wild-type at 3.1 mol% 3HHx. Another mutant R365A lose its ability to incorporate 3HHx in the PHA. R365A do not show any detectable released CoA in the *in vitro* enzyme assay.

[a]Cells were cultivated in 50 mL mineral medium supplemented with 0.054 % urea as nitrogen source at 30ºC, 200 rpm for 48 h. CPKO was added as carbon source at a final concentration of 0.6 %. The values reported are averages from triplicate cultures ± SDs.
[b]Abbreviations: 3HHx, 3-hydroxyhexanoate.

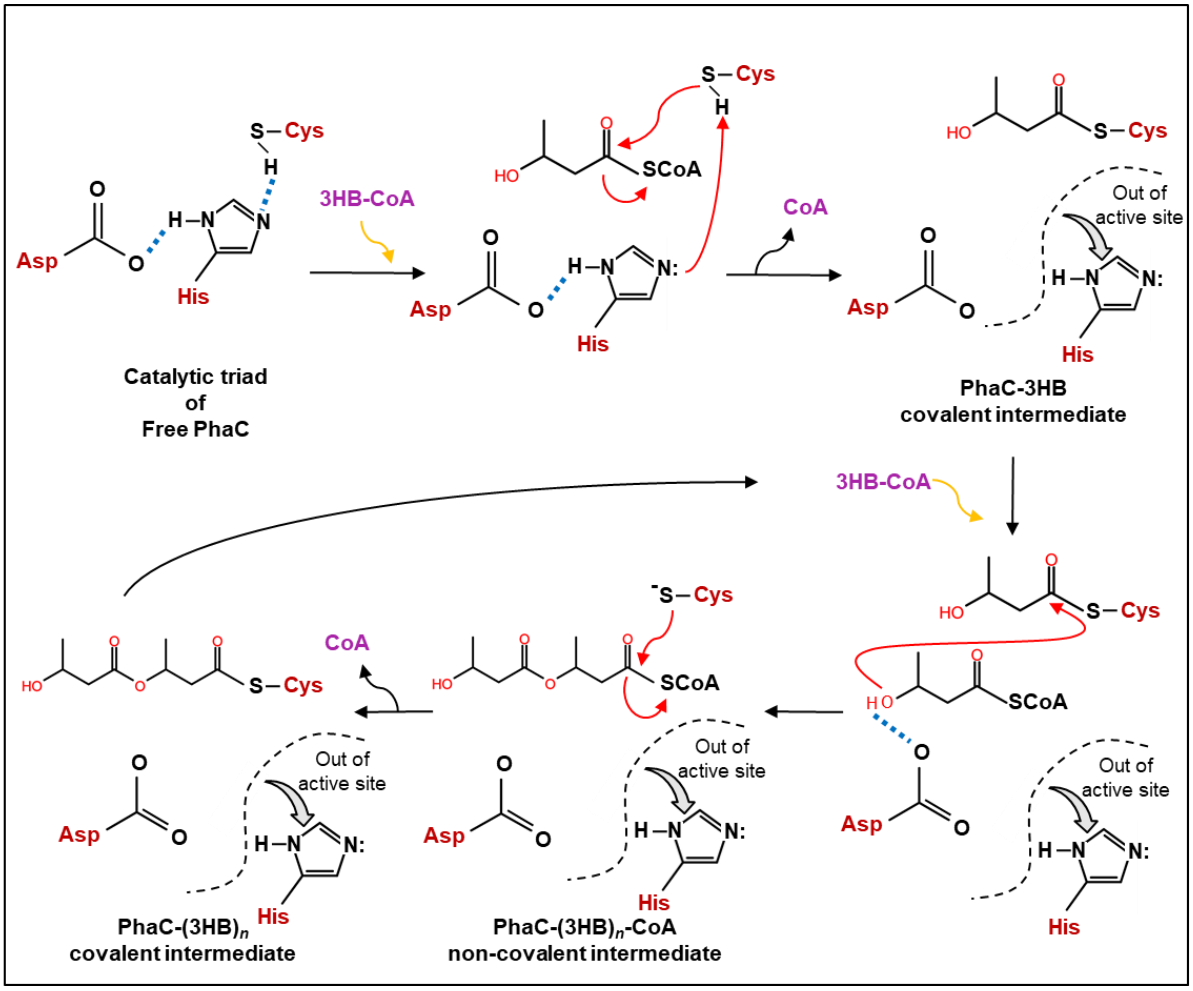

Figure S7. Proposed catalytic mechanism of PhaC, Related to Figure 8D.

(A) This model requires a single active site for PHA chain elongation and a non-covalent intermediate, in addition to a covalent intermediate bound to the Cys residue at the active center during the catalytic cycle. The His477 involved in the initiation but not elongation. The elongated polymer chain will then be growing out from the Site A through the putative product egress, which is sharing a large cleft with the substrate entry pathway.

Table S1. Crystallographic statistics of the CoA-PhaC$_{Cs}$-CAT complex, Related to Figure 2.

Crystallographic Analysis Statistics	
Crystal form	D447N (CoA-bound complex) CoA-PhaC$_{Cs}$-CAT
Space group	*C2*
Unit cell	
a , *b* , *c* (Å)	169.80, 61.85, 82.57
α, *β*, *γ* (°)	90.00, 106.73, 90.00
SPring-8 Beamline	BL41XU
Wavelength (Å)	0.97914
Resolution range [a] (Å)	50.00 – 3.10 (3.15 – 3.10)
Reflections	
Measured/Unique	47983/15234
Multiplicity	3.3 (2.9)
I/σ (*I*)	15.2 (1.7)
R_{merge}(%)	7.9 (51.3)
Completeness (%)	96.5 (87.5)
Refinement Statistics	
R_{work} / R_{free} (%) [b]	22.42/26.27
Number of atoms	5918
Protein molecules	2 (739 residues)
Water molecules	14
Ligand (Coenzyme A)	1
Average B-factors (Å^2)	
Protein	99.50
Water molecules	82.63
Ligand (Coenzyme A)	138.08
R.m.s.d. from ideal values	
Bonds (Å)/ angles (°)	0.004/0.70
Ramachandran plot (%)	
Favored	93.43
Allowed	6.57
Outliers	0.00

[a] Values in parentheses are for the highest-resolution shell.
[b] R_{free} was calculated on a random 5 % reflections of the data.